A Unified Physiological Process Links Global Patterns of Functional MRI, Respiratory Activity, and Autonomic Signaling

Taylor Bolt[1], Shiyu Wang[2], Jason S. Nomi[1], Roni Setton[5], Benjamin P. Gold[3], Blaise deB.Frederick[6], R Nathan Spreng[7], Shella D. Keilholz[8], Lucina Q. Uddin[1]*, Catie Chang[2,3,4]*

[1] Department of Psychiatry and Biobehavioral Sciences, University of California, Los Angeles, Los Angeles, CA, USA

[2] Department of Biomedical Engineering, Vanderbilt University, Nashville, TN, USA

[3] Departments of Electrical and Computer Engineering, Vanderbilt University, Nashville, TN, USA

[4] Department of Computer Science, Vanderbilt University, Nashville, TN, USA

[5] Department of Psychology, Harvard University, Boston, MA, USA

[6] Brain Imaging Center McLean Hospital, Harvard Medical School, Belmont, Massachusetts

[7] Montreal Neurological Institute, Department of Neurology and Neurosurgery, McGill University,Montreal, QC, Canada

[8] Emory University/Georgia Institute of Technology, Atlanta, GA, USA

*Contributed equally

Abstract

Global signal fluctuations are a dominant source of variance in spontaneous BOLD activity. These brain-wide signals co-occur with respiratory and other physiological changes. An often-overlooked possibility is that these physiological associations with global BOLD fluctuations are components of a unified physiological process. Here we combine analysis of multi-modal physiological recordings with simultaneous EEG-fMRI data to demonstrate that global BOLD fluctuations are embedded in a physiological network spanning neural, cardiovascular, pulmonary, exocrine (sweat glands) and smooth muscle (pupil dilator) systems. We further show that these co-fluctuations can be initiated by voluntary changes in respiratory rate and depth. We propose that respiratory variability and its concomitant physiological dynamics are essential explanatory ingredients in the origin of global BOLD fluctuations.

Introduction

Widespread fluctuations of cerebral blood flow and oxygenation occur spontaneously in the resting human brain (Obrig et al., 2000). These global fluctuations appear as a dominant

source of spontaneous low-frequency (~0.01-0.1Hz) fluctuations in blood-oxygen level dependent (BOLD) signals recorded by functional magnetic resonance imaging (fMRI) (Fox & Raichle, 2007; Liu et al., 2017). The first principal component of spontaneous BOLD signals tracks these global fluctuations, explaining a large proportion of variance in spontaneous BOLD signals (Bolt et al., 2022). Due to its ubiquitous presence, delineating the neurophysiological mechanisms underlying these global fluctuations is a central concern for both neuroscientists and physiologists.

Fluctuations in respiratory depth and rate have been proposed as a significant source of global BOLD fluctuations in resting-state fMRI signals (Birn et al., 2008; Power et al., 2017; Wise et al., 2004). However, several other other physiological signals are correlated with global BOLD fluctuations, including autonomic nervous system (ANS)-mediated signals and electrocortical signals from surface and intracranial electroencephalography (EEG). ANS-mediated physiological signals associated with global BOLD include peripheral vascular tone (Özbay et al., 2019; Tong et al., 2012), sudomotor activity (i.e. skin conductance; Fan et al., 2012; Gertler et al., 2020), heart rate (Chang et al., 2009; de Munck et al., 2008; Shmueli et al., 2007), and pupil diameter (Pais-Roldán et al., 2020; Yellin et al., 2015). Fluctuations in oscillatory power in surface EEG and local field potential (LFP) recordings have also been associated with global BOLD signal (Schölvinck et al., 2010; Wen & Liu, 2016; Yuan et al., 2013). Taken together, these observations suggest that global BOLD fluctuations contain a mix of respiratory, autonomic, and neural signals.

An often overlooked possibility is that these electrophysiological associations with global BOLD fluctuations are components of a unified physiological process closely organized in time. We propose that variations in respiratory rate and depth are a key regulator of this process. Low-frequency (<0.1 Hz) variations in respiratory depth and rate are associated with fluctuations in end-tidal CO2 (Chang & Glover, 2009; Wise et al., 2004), but this relationship is one component of a much larger cascade of downstream effects on multiple physiological systems. It is well established that variations in respiration rate and depth induce prominent fluctuations in direct recordings of sympathetic motor neurons (Häbler et al., 1994). Sympathetic outflow due to respiratory inhalation mediates a wide-variety of physiological dynamics: increased heart rate (i.e. respiratory sinus arrhythmia; Yasuma & Hayano, 2004), increased vasoconstriction in the peripheral vasculature (Khoo & Chalacheva, 2019; Malpas, 2010), increased pupil diameter (Ohtsuka et al., 1988), and increased sudomotor activity (i.e. skin conductance; though this relationship may depend on ambient temperature; Bini et al., 1980; Jänig et al., 1980). These physiological changes include respiration-driven changes in scalp EEG and local field potentials (Kluger & Gross, 2021; Shams et al., 2021; Tu & Zhang, 2022; Zelano et al., 2016). Consistent with these findings, resting-state fMRI studies have observed concomitant fluctuations between global BOLD signals, respiratory variance and one or more of these physiological signals (Gu et al., 2022; Yuan et al., 2013).

In this study, we explore the global BOLD response to spontaneous and voluntary respiratory fluctuations with multi-modal physiological and EEG recordings. The physiological signals considered and their associated datasets are presented in **Figure 1**. We demonstrate

that spontaneous fluctuations in global BOLD are organized into a single, joint co-fluctuation with respiratory variance and several ANS-mediated physiological signals, including heart rate, peripheral vascular tone, pupil dilation and fluctuations in oscillatory EEG power. We then show that periods of voluntary deep breathing induce similar dynamics in BOLD and ANS-mediated physiological signals, including measures of skin conductance. This shared physiological response explains a range of previously observed associations between global BOLD fluctuations, respiratory variance and other physiological signals. These findings have implications for understanding the neurophysiological mechanism underlying global BOLD fluctuations and implicate a plausible vascular or neurogenic role of ANS signaling in the generation of global BOLD fluctuations.

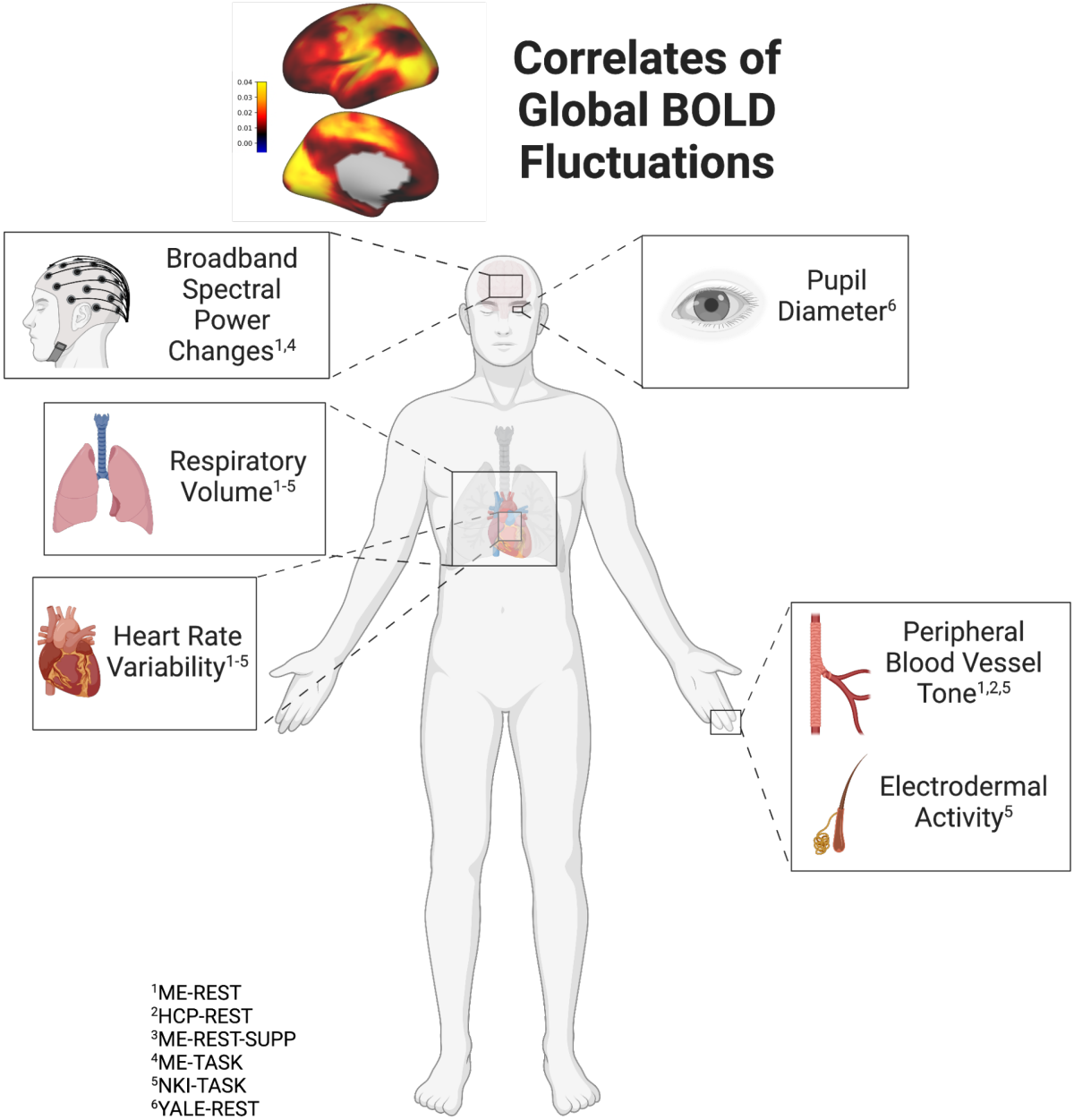

Figure 1. **Physiological Signals Associated with Global BOLD Fluctuations.** Physiological signals that have been previously associated with global BOLD fluctuations. The cortical surface map in red-yellow coloring at the top of the illustration displays the spatial weights of the first principal component of cortical BOLD signals. Six datasets were included in this study to 1) expand the pool of physiological signals considered, and 2) allow replication of findings. Each physiological signal is appended with superscript numerals referencing the dataset(s) that measured those signals. The labels used to reference each dataset are displayed in the bottom left of the illustration (further details on each dataset are provided in the Methods section).

Results

The Dominant Spatiotemporal BOLD Pattern Covaries In Time with Multiple Physiological Signals

The first principal component of low-frequency (0.01 - 0.1 Hz) BOLD time courses represents a widespread pattern of global BOLD activity in gray matter. Analysis of the time-lag structure of this global pattern of BOLD activity via complex-valued PCA (CPCA) on the cortical surface revealed an orderly sequence of BOLD activity across the cortex (Bolt et al., 2022). The pattern begins with an early peak of BOLD amplitudes in the somatomotor, lateral visual and auditory cortices, followed by peaks of BOLD amplitude in the precuneus, lateral prefrontal cortex, anterior cingulate cortex, inferior parietal and primary visual cortex. This pattern of global BOLD activity was found to track the average gray matter BOLD time course (Bolt et al., 2022). For consistency with previous literature, we refer to this pattern and its representation in the first principal component (in both PCA and CPCA), as the 'global BOLD signal'. The first principal component and first complex principal component for all datasets used in this study are presented in **Supplementary Figure 4**.

Analysis of four separate resting-state fMRI datasets (ME-REST, HCP-REST, ME-REST-SUPP and YALE-REST) shows that the time course of the global BOLD signal (extracted via the first principal component) covaries with several peripheral electrophysiological signals (CNS) (**Figure 2**). For almost all electrophysiological signals and datasets, the strongest correlation observed between global BOLD signal and the electrophysiological signal is at a positive or zero lag of the global BOLD signal, meaning these signals lead, or co-occur with, the global BOLD signal, respectively.

Spontaneous fluctuations in respiratory volume (RVT), heart rate (HR), peripheral vasculature (low-frequency PPG and PPG pulse amplitude) and pupil dilation signals show strong correlations with the global BOLD signal (**Figure 2C**). Consistent with previous reports of an anti-correlated dynamic between global gray matter BOLD signals and cerebrospinal fluid (CSF) signals (Gonzalez-Castillo et al., 2022; Picchioni et al., 2022), the spatial weights of the global BOLD signal (PC1; **Figure 2A**) from the ME-REST and HCP-REST datasets encode an anti-correlated fluctuation between voxels of the ventricles and those of the gray and white

matter. Consistent with this pattern, correlations between the time courses of ventricle BOLD signals and the global BOLD signal exhibit strong anti-correlation across subjects (**Figure 2C1**). However, the anti-correlation between BOLD signals from the CSF and gray/white matter is not observed for the YALE-REST dataset. Global BOLD signals are also associated with wide-band (2 - 20Hz) fluctuations in EEG power (**Figure 2D**). Strong cross-correlations are observed across all frequencies, but the largest magnitude correlations are observed at higher frequencies (> 10Hz).

The time-lag structure of the global BOLD signal revealed by complex PCA (CPCA) exhibits a consistent propagation pattern across datasets, with early BOLD amplitude increases in superior central regions (e.g. midline sensory/motor cortex), followed by signals in posterior draining sinuses and late signals in the cerebrospinal fluid (CSF) compartments (**Figure 2B1**). The time-lag structure of the global BOLD signal also resembled the voxel-wise cross-correlation delays with low-frequency (0.01-0.1Hz) peripheral blood volume signals (low-frequency PPG; **Figure 2B2**), the same cross-correlation pattern observed in previous studies (Tong et al., 2012). Frame-by-frame temporal reconstructions (see Methods) of the time-lag dynamics of the first BOLD complex principal component are displayed for the ME-REST and HCP-REST datasets in **Supplementary Movies 1** and **2**.

These cross-correlations establish pairwise relationships between globally structured BOLD signals and multiple electrophysiological signals, but do not provide definitive evidence of a unified joint co-fluctuation across all signals in time. We performed a cross-decomposition between all pairs of signals and their lags via multi-set canonical correlation analysis (MCCA; see Methods). Our aim was to examine whether the joint co-fluctuations between all signals (and their time-lags) can be extracted in a single latent component. Application of MCCA to ME-REST dataset demonstrates that the first canonical component (**Figure 2E**), representing the latent component with the maximal average pairwise correlation between all pairs of signals, captures strong pairwise correlations between all pairs of electrophysiological signals ($\underline{r}$ = 0.31, p = 0.001). Further, the global BOLD signal (PC1) exhibits the strongest pairwise correlations among all signals within the first canonical component. These results were replicated for HCP-REST ($\underline{r}$ = 0.25, p = 0.001) and ME-REST-SUPP (r = 0.24, p = 0.001) datasets. The MCCA results for all three resting-state fMRI datasets are presented in **Supplementary Figure 3**.

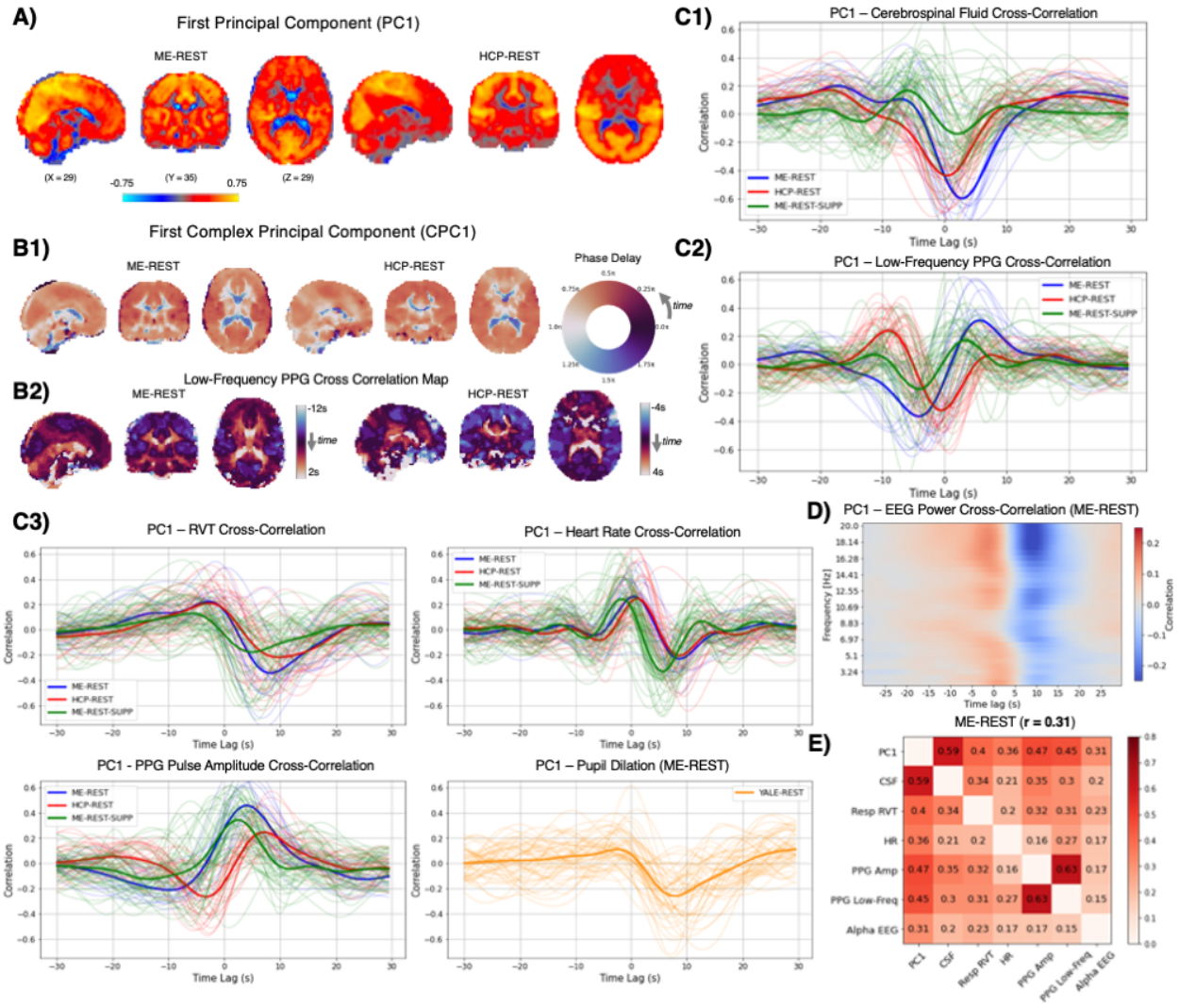

Figure 2. **Joint Fluctuations Between Global BOLD Signals and Electrophysiological Signals. A)** The spatial weights of the first principal component (PC1) for the ME-REST and HCP-REST datasets (slice indices are in voxel 3mm coordinates). **B)** The time-lag structure of the first complex principal component (CPC1; **B1**) exhibits a propagation pattern resembling the pattern of time-lags between voxel-wise BOLD signals and low-frequency peripheral blood volume signals (**B2**) (Tong et al., 2012). The phase delay map (in radians) of CPC1 is displayed in a circular color map. The maximal cross-correlation time-lag between the low-frequency peripheral blood volume signals and voxel BOLD time courses is displayed below the CPC1 phase delay maps. **C1)** The cross-correlation between the time courses of the first principal component and the average BOLD signal of the ventricles in the ME-REST (blue), HCP-REST (red) and ME-REST-SUPP (green) datasets. All subject-level cross-correlations are displayed in lighter, more transparent color, while the mean signal across subjects is displayed in a darker color. Positive time lags indicate that the PC1 time course lags that signal, while negative time lags indicate that the PC1 time course leads that signal. **C2**) Cross-correlations between the PC1 time course and the low-frequency peripheral blood volume signal (low-frequency PPG). **C3)** Cross-correlations between the PC1 time course and respiratory volume (RVT), heart rate, PPG pulse amplitude and pupil dilation. **D)** For EEG power in the ME-REST dataset, cross-correlations between wavelet filtered EEG power signals (Morlet wavelet; number of cycles = 15) and PC1 are displayed as a heat map. **E)** The pairwise correlations between all electrophysiological signals (including PC1) in the first canonical variate of the

MCCA analysis for the ME-REST dataset. Note, though the relationship between global BOLD and EEG power is broadband (see **panel D**), we included Alpha (8-12Hz) EEG power as a single signal from the EEG due to previous reports of a relationship between Alpha power and global BOLD signals (Yuan et al., 2013). The darker colors indicate stronger correlation. The average pairwise correlation is displayed beside the title (in bold) of each correlation matrix. The pairwise correlations of the first canonical variate indicate a strong, joint co-fluctuation between all electrophysiological signals and PC1.

Voluntary Respiration Changes Elicit a Reliable Sequence of BOLD-Physiological Joint Co-Fluctuations

We hypothesized that low-frequency respiratory variance (i.e. changes in respiratory depth and/or rate) is a common driver of global BOLD, EEG and physiological co-fluctuations during resting-state fMRI scans. To provide empirical support for this model, we performed analyses on two respiration task datasets, including a cued deep inspiration task (ME-TASK) and a paced breathing/breath-hold task (NKI-TASK).

Global BOLD (PC1) and CSF signals exhibit large amplitude fluctuations to single deep breaths (ME-TASK) (**Figure 3A**). Consistent with the shape of the respiration response function described by Birn et al. (2008), global BOLD signals exhibit a bimodal response to inspiration, with an early positive increase (~4s) followed by a prolonged undershoot reaching its trough around ~14s. Consistent with the anti-correlated dynamic observed in resting-state, BOLD signals averaged from the ventricles (CSF) show a small magnitude increase around the same time PC1 time course reaches its trough (~14s). Global BOLD signals and CSF fluctuations in the paced deep breathing period of the breath-hold task (NKI-TASK) exhibit similar dynamics with an early positive increase in global BOLD signals, followed by a prolonged undershoot in the latter portion of the breath-hold block (**Figure 3B**). Interestingly, the amplitude of the early positive increase is smaller following periods of prolonged breath holds, appearing as positive 'bumps' interrupting the return to baseline from the breath hold block.

Electrophysiological signals exhibit temporal dynamics consistent with increased ANS activity after the onset of voluntary respiratory fluctuations (**Figure 3A**). These dynamics can be split into two phases, similar to the bimodal response of global BOLD signals to respiration fluctuations. Around the same time as the early (~4s) positive peak of the respiration response, changes in peripheral blood volume, heart rate, broadband EEG power (ME-TASK) and skin conductance (NKI-TASK) are observed post inspiration. The increase in heart rate following inspiration, and the subsequent decrease around ~8s, is consistent with gating of parasympathetic outflow (via the vagus nerve) during inspiration and its relaxation during exhalation, known as respiratory sinus arrhythmia (Yasuma & Hayano, 2004). Low-frequency peripheral blood volume exhibits a decrease around the positive peak, indicative of vasoconstriction of peripheral blood vessels by sympathetic outflow (Khoo & Chalacheva, 2019). The decrease in peripheral blood volume exhibits smaller amplitudes when it is preceded by prolonged breath holds (NKI-TASK). Increases in tonic skin conductance (SC) signals (NKI-TASK) are observed around the early peak of the respiration response, indicative of a sympathetic-mediated increase in sudomotor activity.

Later peaks of electrophysiological signals occur around the time of the undershoot of the global BOLD signal (~14s). Around the time of the undershoot (~14s), heart rate rebounds to a similar rate to that observed following the first inspiration. Peripheral blood volume also exhibits a positive peak around the time of the undershoot (~14s).

The prolonged breath hold in the breath hold task (NKI-TASK) induces a large magnitude increase in global BOLD signals peaking several seconds after the end of the breath-hold (e.g., time point 32). The prolonged breath hold induces a strong amplitude decrease in heart rate and increase in peripheral blood volume. The time courses of the global BOLD signal (PC1) do not appear to show a robust early phase marker in breath-hold trials as do the time courses to inspiration (e.g. the slight positive 'bumps' mentioned above).

The isolated deep breaths in the ME-TASK and consecutive deep breaths in the NKI-TASK are characterized by both an increase in respiratory depth (amplitude) and a decrease in respiratory rate. We sought to determine which component of these deep breaths were most predictive of global BOLD fluctuations in resting-state fMRI conditions measured by a respiration belt. We separately extracted the depth/amplitude and instantaneous frequency (respiration rate) components of the respiratory volume (RVT) time course (see Methods). For each subject in all three resting-state datasets, the PC1 time course was then regressed onto the respiration amplitude and respiration rate (and their time lags). For each subject, the unique and common variance explained by respiration depth and respiration rate was partitioned out of the total explained variance (see Methods). Analyses for all three resting-state datasets (ME-REST, HCP-REST, and ME-REST-SUPP) suggests that the depth/amplitude of the respiration belt signal is the most prominent factor in explaining spontaneous fluctuations in global BOLD fluctuations, over and above the contribution of respiration rate and the variance shared in common with respiration rate (**Figure 3C**).

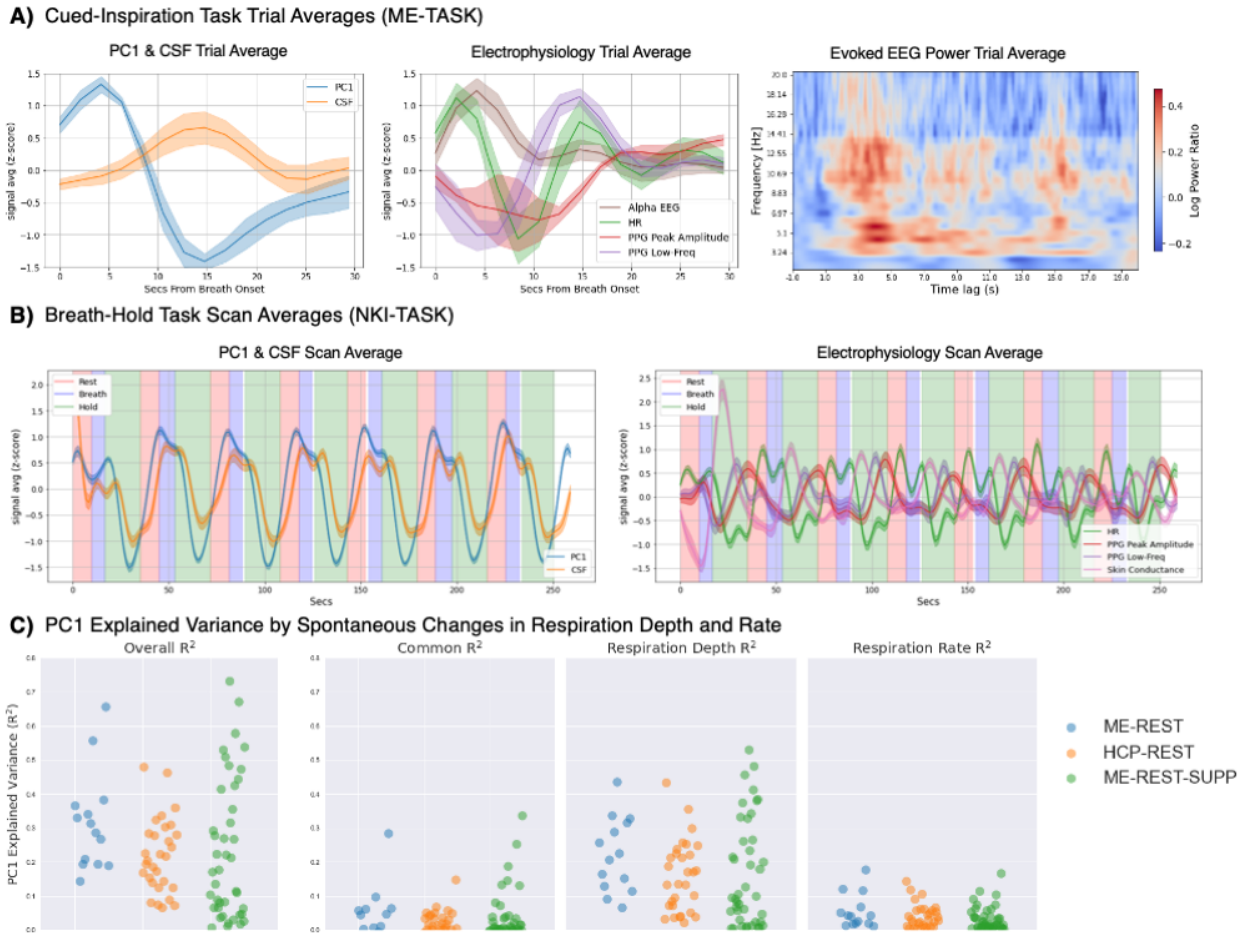

Figure 3. **Voluntary Inspiration and Breath-Holding Generate Joint BOLD-Physiological Co-Fluctuations. A)** Deep inspiration in response to an auditory cue (ME-TASK) induces large magnitude fluctuations (for many signals, >=1 standard deviation) in global BOLD (PC1) and electrophysiological signals. Trial-averaged responses to deep inspiration across subjects for PC1 and CSF time courses (left), electrophysiological signals (middle) and evoked EEG power (right). Standard error bars for the left and middle plot time courses are constructed via cluster bootstrapping (i.e. resampling at the subject level; # of samples = 100). Evoked EEG power trial averages were constructed through trial-averaging of Morlet wavelet filtered power signals within subjects (see Methods), followed by group-averaging across subject-trial averages. Before group-averaging, evoked EEG power changes at the subject-level were baseline normalized (log-ratio) from the preceding 1 sec before stimulus onset. **B)** The scan-averaged time course across all subjects for global BOLD (PC1) and CSF (left) signals, and electrophysiological signals (right) of the NKI-TASK dataset. Task blocks are colored according to their block type (red: rest, blue: deep breathing, breathe hold: green). As with trial averages in the ME-TASK dataset, standard errors are generated with cluster bootstraps. The scan-averaged time courses of PPG-derived heart rate, vasculature and tonic skin conductance signals (no EEG signals were collected) in the NKI-TASK dataset. **C)** Plots displaying the separate contributions of respiratory depth (amplitude) and respiration rate of respiration belt signals to spontaneous fluctuations in PC1 across the three resting-state datasets. For each subject, PC1 time courses are regressed onto regression rate and amplitude (and their time lags), and the explained variance (R2) partitioned into separable and common contributions. The y-axis is shared across all four plots, and displays the explained variance estimate of each component for each subject (displayed as a dot). Within each dataset, subject explained variance estimates are randomly scattered along the x-axis for visual separation.

The Relationship between the Global BOLD Signal and Respiration is Modulated by Vigilance States

Previous research has established that the amplitude of low-frequency fluctuations in global BOLD and CSF signals is not constant across time, but non-stationary. This non-stationarity seems to be related to changes in vigilance states across the course of the scanning session (Fultz et al., 2019; Picchioni et al., 2022). For the ME-REST dataset, we tracked low-frequency changes in vigilance state using a sliding-window (105s; 50 time points) average of an EEG-derived vigilance index (see Methods) across the course of the scan. To track low-frequency amplitude changes in global BOLD and CSF, we computed the variance of the time courses within a sliding window (105s) across the course of the scan. Sliding window variance time courses of global BOLD and CSF signals reveal alterations between high-amplitude and low-amplitude regimes over the course of the scan for most subjects (**Figure 4A**). Further, these high amplitude regimes of global BOLD and CSF time courses occur more frequently during low-vigilance states (PC1: $r = -0.40$, CSF: $r = -0.42$, $p = 0.001$).

Increased coupling between global BOLD and physiological signals during low vigilance states and arousal transitions has also been observed (Gu et al., 2022; Soon et al., 2021). Given the previously established relationship between respiratory variance and global BOLD signals, these findings suggest that global BOLD autonomic-coupling should be more prominent during low vigilance states. To examine this possibility, we used a regression-based interaction analysis with global BOLD (PC1) time courses regressed on respiratory volume signals and low-frequency vigilance states (< 0.01Hz), and their interaction. Low-frequency vigilance states had a negative interaction effect between global BOLD time courses and respiratory volume ($p = 3.91e-06$), such that the covariation between global BOLD time courses and respiratory volume increased during low vigilance states (**Figure 4B**). Analysis of this interaction effect across different window sizes (42s - 168s) demonstrates that the results are robust to the width of the window, with stronger interaction effects at longer window sizes (**Figure 4B**).

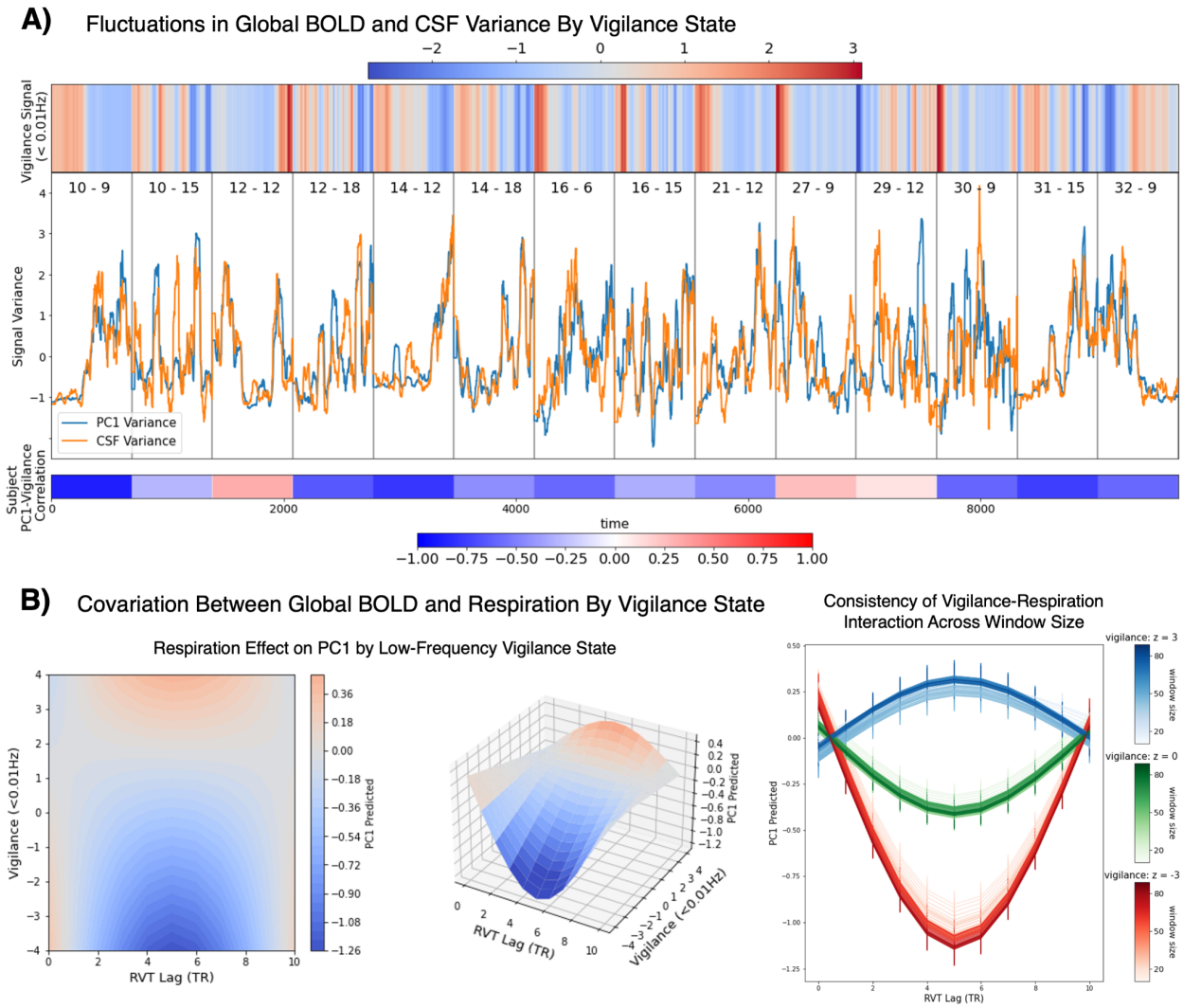

Figure 3. **Modulation of Global BOLD Signals and Respiratory Fluctuations by Vigilance State.** A) The sliding window time courses of CSF and BOLD signal variance temporally concatenated across all subjects in the ME-REST dataset. Note, these time courses are not centered/normalized within subjects to allow visualization of baseline differences in PC1/CSF amplitudes across subjects. PC1 and CSF sliding window variance time courses are displayed in the middle of the plot (blue and orange, respectively). Vertical bars are displayed to mark the transition from one subject's time courses to the next. Subject - scan labels are displayed above each time course. Sliding window average vigilance time courses across subjects are displayed as a heat map above the PC1/CSF time courses, with lower values as dark blue and higher values as dark red. Subject correlations between vigilance and PC1 sliding window time courses are displayed below the time course plot aligned with their respective subject-scan. Correlation coefficients per subject-scan are illustrated with a color map, where strong positive correlations are displayed in red and strong negative correlations in blue. **B)** Display of the interaction effect between respiratory volume (RVT) and PC1 fluctuations by vigilance state. The plots to the left display the predicted PC1 score (in z-score units) as a function of 1) lags of the RVT time course and 2) sliding window mean vigilance values (in z-score units). These plots are displayed in 2D (left) and 3D (right) format. The plot to the right displays the predicted PC1 value as a function of lags of the RVT time course and a specific value (z-score) of vigilance, including z=-3 (red), z=0 (green) and z=3 (blue).

linear beta coefficients between PC1 and respiration amplitude time courses at a selected value of vigilance (top: z-score=4, bottom: z-score=-4). These plots demonstrate that the relationship between respiratory fluctuations and PC1 time courses are strongest at low vigilance levels.

The Spatiotemporal Structure of Hemodynamic Responses to Fluctuations in Respiratory Volume

Previous analyses have treated global BOLD fluctuations as a single time course - the time course of the first principal component (PC1). As shown in Bolt et al. (2022), global BOLD fluctuations exhibit a well-defined spatiotemporal structure with a consistent pattern of BOLD signal propagation across the cortex (see also, **Figure 1**).To demonstrate that the hemodynamic response to respiratory volume fluctuations exhibits the same spatiotemporal structure, we used mass-univariate regression modeling. We fit voxel-wise regression models to the resting-state BOLD time courses using spline bases for the time-lag and amplitude components of the respiratory volume time course (Gasparrini et al., 2010). The fitted models at each voxel were evaluated at different magnitudes of respiratory volume (0.5 - 2.5 in z-score units). Evaluation of predicted BOLD responses at each voxel across lags (-10 - 30s) of the respiratory volume time course generates a hemodynamic response across time. A similar approach using peak-averaging around windows of high respiratory volume generated a similar hemodynamic response (**Supplementary Movie 3**).

First, we examined the dynamics of the global hemodynamic response to a range of spontaneous respiratory volume fluctuation magnitudes (z = 0.5-2.5; in z-score units). (**Figure 4A**). Global hemodynamic responses were constructed by averaging predicted BOLD responses across gray matter voxels. Across all three resting-state fMRI datasets, the global hemodynamic response was largely constant in shape across respiratory volumes, with a magnitude proportional to the respiratory volume. The shape of the global hemodynamic response to spontaneous fluctuations in respiratory volume paralleled the hemodynamic response to deep inhalations in the ME-TASK dataset (**Figure 3A**): an early positive overshoot of global average BOLD signals (-4s) followed by a larger magnitude undershoot (10s).

Examination of the hemodynamic response to increased respiratory volume (i.e. increased respiratory depth and/or rate) across three resting-state fMRI datasets shows a consistent spatiotemporal pattern with some timing variability (**Figure 4A**). The early positive overshoot at the beginning of the hemodynamic response (-4s) is marked by increased BOLD signals across the gray and white matter, and decreased BOLD signals in the ventricles. This is followed by a transition phase characterized by two dynamics: 1) propagation of increased BOLD signals towards the cingulate cortex, precuneus, ventricles and large draining veins and 2) decreased BOLD signal in the sensory-motor, visual and medial prefrontal cortex. Around the time of the later negative undershoot (~10s) the decreased BOLD signals observed in the transition phase have expanded to all gray and white matter tissues.

Trial-averaging of respiratory inspiration trials in the respiration task fMRI datasets (ME-TASK and NKI-TASK) show a similar spatiotemporal structure to the hemodynamic response to spontaneous respiratory volume (**Figure 4C**). However, in the case of task-fMRI datasets, inhalations are aligned to stimulus cues with known timing. Around 4-7s post-inhalation, increased BOLD signals are observed across gray and white matter tissues and decreased BOLD signals in the ventricles, followed by a transition phase resembling the dynamics observed in the spontaneous hemodynamic response (**Figure 4B**), and finally decreased BOLD signals across the gray and white matter.

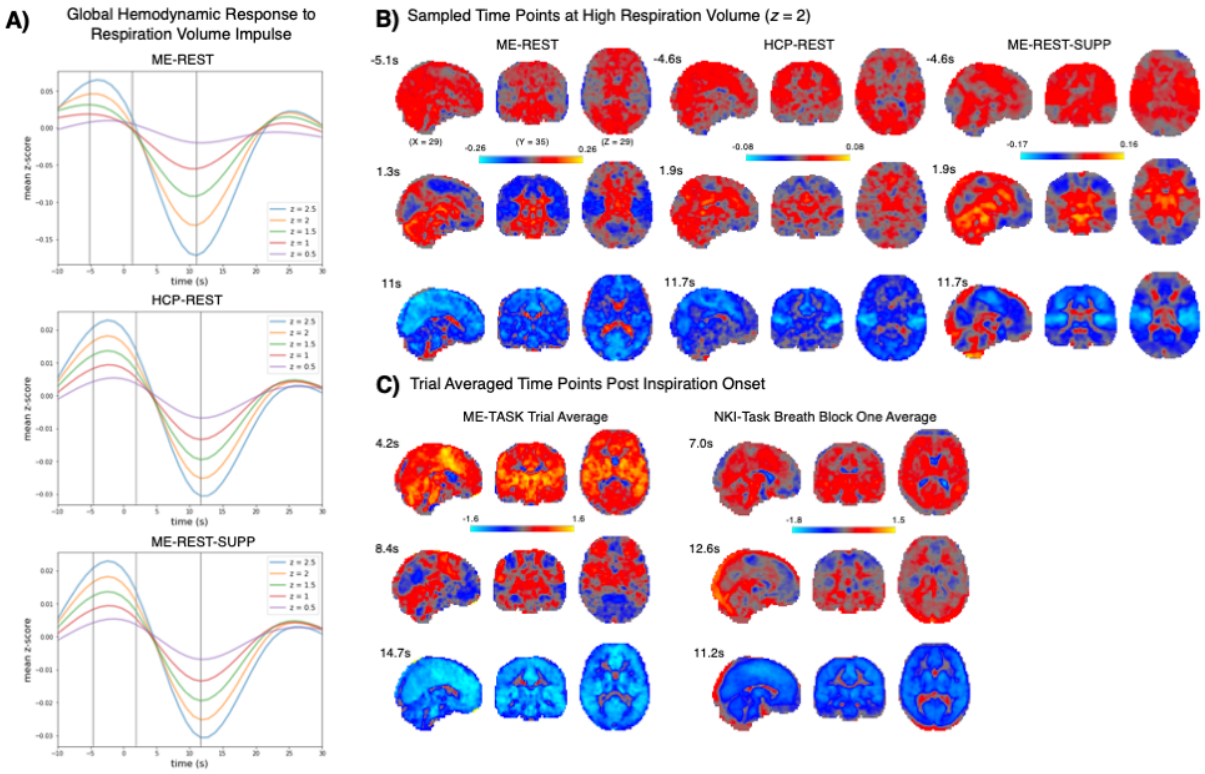

Figure 4. **The Hemodynamic Response to Spontaneous and Voluntary Changes in Respiratory Volume Has a Complex Spatiotemporal Structure. A)** The global average hemodynamic response to different magnitudes of respiratory volume (z = 0.5 - 2.5; z-score units) across all three resting-state fMRI datasets. For all three datasets, the shape of the hemodynamic response is largely constant across respiratory volume magnitudes. **B)** Whole-brain BOLD values at different time points of the hemodynamic response to respiratory volume at z = 2. Time points are in time lags of the BOLD response to the respiratory volume time course (e.g. 2s corresponds to a lag of the respiratory volume time course by 2s 'forward' in time). Note, predicted BOLD values are in z-score units. **C**) The hemodynamic response to the cued-inspiration (ME-TASK) and selected deep breathing block (block one; NKI-TASK) derived by trial averaging across subjects. The time (in seconds) post-onset is displayed beside each map. Note, the NKI-TASK is post-onset from the start of the 'breath' block that occurred before the breath-hold.

To compare whether the hemodynamic response to respiratory volume recapitulates the same spatiotemporal structure as spontaneous global BOLD fluctuations, we computed a temporal reconstruction of CPC1 (see Methods) from the ME-REST dataset and examined its temporal evolution (**Figure 5A; Supplementary Movie 1**). Visual examination of the reconstructed time points revealed the same temporal sequence as that observed in response to increased respiratory volume: a global increase in BOLD signals, followed by a bimodal pattern of activity, and then a global decrease in BOLD signals. Spatial correlations of the time points from the temporal reconstruction of CPC1 and the phases of the hemodynamic response to increased respiratory volume also revealed considerable overlap (global positive pattern: r = 0.67, bimodal pattern: r = 0.87, global negative pattern: r = 0.94).

The hemodynamic response to respiratory volume and global BOLD fluctuations exhibit a characteristic pattern of BOLD propagation across the brain: increased BOLD signals propagate outward towards the dorsal and posterior midline, and inwards to the cingulate cortex and ventricles. This propagatory behavior of the temporal dynamics of CPC1 is most easily seen in movies of the dynamic (**Supplementary Movie 1**; HCP-REST dataset: **Supplementary Movie 2**). The direction of this propagation is towards areas overlapping with locations of large draining veins, including the superior sagittal sinus, inferior sagittal sinus, straight sinus and the vein of Galen. Comparison of the bimodal pattern of BOLD activity with large cerebral vein/artery vessel atlases (Viviani, 2016; Ward et al., 2018) confirms this overlap (**Figure 5B**). This propagation of BOLD signals towards sites of large cerebral veins likely reflects downstream propagation of pooled blood oxygenation changes in the microvasculature (e.g. due to local changes in neural activity) during the globally positive pattern.

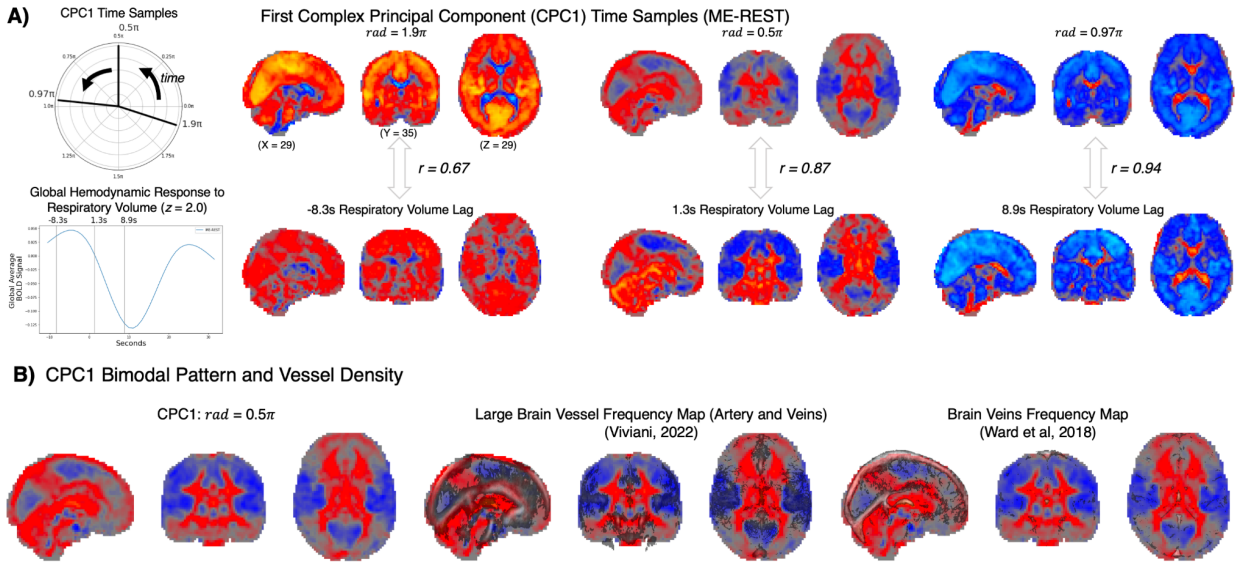

Figure 5. **The Hemodynamic Response to Respiratory Volume Maps Onto the Spatiotemporal Pattern of Global BOLD Fluctuations.** The temporal sequence of the first

complex principal component (CPC1) recapitulates the temporal dynamics observed in the respiration response to respiratory volume in the ME-REST dataset. **A)** Three time samples selected from a temporal reconstruction of CPCA (rad = 1.9π, 0.5π, 0.97π; note, radians are circular units in the span from 0 to 2π) are displayed in the top panel. The selection of the time samples from the CPCA temporal reconstruction are illustrated on a unit circle, and their temporal progression is illustrated by three consecutive lines (moving counter-clockwise) corresponding to selected samples. The bottom panel displays three matched time samples from the predicted BOLD activity patterns following peak respiratory volume (z=2.0) in spontaneous BOLD signals (**Figure 4).** The spatial correlation between the CPC1 time points and predicted BOLD activity patterns are displayed besides the bi-directional arrows. The average hemodynamic response (across gray matter voxels) is displayed for reference (the time in seconds of each matched sample is displayed as vertical lines in the plot). **B)** The bimodal CPC1 time pattern (rad = 0.5π) with overlaid (transparent) large brain vessel atlases (Viviani, 2016; Ward et al., 2018). The middle panel displays a time-of-flight (TOF) MRI frequency atlas of large cerebral vessels (arteries and veins; Viviani, 2016). The right panel displays a combined susceptibility-weighted image (SWI) and quantitative susceptibility image (QWI) MRI atlas of large cerebral veins (Ward et al., 2018). High positive amplitude regions of the bimodal CPC1 pattern are observed along the dorsal midline of the brain, the cingulate cortex and the space between the occipital lobe and cerebellum (tentorium cerebelli), which overlap with areas of the brain innervated by large draining veins.

Discussion

Global whole-brain fluctuations represent the dominant source of variance in spontaneous BOLD fMRI signals (Bolt et al., 2022). This study demonstrates that global BOLD fluctuations are embedded in a physiological network spanning neural, cardiovascular, pulmonary, exocrine (e.g. sweat glands) and smooth muscle (e.g. pupil dilator muscle) systems. These results suggest that previously observed relationships between global BOLD signals and physiological signals are reflective of a single, underlying neurophysiological event or process. We found that voluntary changes in respiratory volume (respiration rate and depth) are a sufficient cause of these brain-body fluctuations. Further, the spatiotemporal structure of BOLD fluctuations in response to voluntary changes in respiratory volume match those observed in spontaneous global BOLD fluctuations.

We observe that global BOLD and physiological signals in response to deep breathing exhibit the following temporal sequence (**Figure 2**): 1) increased heart rate (~2s), consistent with parasympathetic outflow via vagal nerve motor neurons (Yasuma & Hayano, 2004), 2) shortly following the increased heart rate, there are increased global BOLD signals, skin conductance (sudomotor activity) and broadband EEG power, along with peripheral vasoconstriction (~4s). The latter three signals are consistent with an increased state of

subcortical arousal and sympathetic nervous system outflow. This is followed by 3) a decrease in heart rate (~8s), followed shortly by decreased global BOLD signals and peripheral vasodilation (~14s). While pupil diameter signals were only recorded in resting-state conditions, the cross-correlation analysis (**Figure 1**) suggests that increased pupil dilation occurs around the time of the global BOLD signal overshoot (~4s), consistent with inhibition of parasympathetic-mediated outflow to the iris constrictor muscles and excitation of sympathetic-mediated outflow to the iris dilator muscle (Marumo & Nakano, 2021).

Several characteristics of global BOLD fluctuations observed in this study are worth noting. First, is the anti-correlated fluctuations in BOLD signals observed between gray/white matter tissue and ventricles (**Figure 1**). While our study did not explicitly measure CSF inflow effects (Fultz et al., 2019), these findings are consistent with anti-correlated fluctuations observed between the CSF (measured from an ROI in the fourth ventricle) and global BOLD signals that become more prominent during periods of low vigilance (Gonzalez-Castillo et al., 2022; Picchioni et al., 2022). Second, is the time-lag or traveling wave structure of spontaneous global BOLD fluctuations and those observed in response to voluntary respiratory changes. As in Bolt et al. (2022), we show that the spatiotemporal pattern of global BOLD fluctuations is marked by a well-defined propagation of BOLD signals across the cortex (**Figure 2; Figure 4; Figure 5**). In this study, we find that this propagation behavior extends well into the subcortex and CSF compartments. This propagation behavior is characterized by the propagation of BOLD signals outward towards the dorsal and posterior midline, and inwards to the cingulate cortex and ventricles. We find that this pattern of BOLD propagation aligns well with the pattern observed in systemic low-frequency oscillations (Tong et al., 2012) constructed from cross-correlations with signals from the peripheral vasculature. Consistent with Tong et al. (2012), we found a similar propagation pattern from cross-correlation with low-frequency (0.01-0.1Hz) photoplethysmography recordings from the fingers. Third, the 'final' destination of these propagatory BOLD signals is in areas of the brain densely innervated by large draining veins (e.g. superior sagittal, inferior sagittal and straight sinus). It is important to note the propagation of global BOLD fluctuations towards cortical veins does not imply a vascular or non-neurogenic cause of global BOLD fluctuations. The BOLD contrast is biased towards large veins (Menon, 2002), and large veins will contribute strongly to the observed BOLD signal when proximal to sites of task-driven oxygenation changes. In the hypothetical case of a neurogenic origin of global BOLD fluctuations, large-scale increases in BOLD contrast across the cortex will inevitably have a strong vessel contribution at a positive time lag from the onset of neural-driven oxygenation changes in the microvascular (capillaries and small venules). This consistent time lag in BOLD increases between microvascular and large veins informs methods for the latter's removal from BOLD signals (Kay et al., 2020).

To situate our findings in the broader human neuroimaging literature, it is helpful to introduce the notion of causal proximity in the form of proximate and distal causal mechanisms. Proximate causal mechanisms represent the mechanisms 'closest to' or most 'immediate' to the production of a phenomena, while distal causal mechanisms represent mechanisms further removed or 'remote' from the phenomena but still important in its production. It is immediately clear that a deep respiratory inspiration is not a proximal cause of global BOLD fluctuations, but

act by an intervening, more proximal cause, such as changes in arterial CO2, sympathetic vasoconstriction, projections of subcortical nuclei, or mechanosensory/visceral afferent activity. Our findings establish respiratory volume fluctuations as a potential distal cause of global BOLD fluctuations, but do not determine a definite proximal cause. Further, it is possible that respiratory volume fluctuations represent only one distal cause mechanism of global BOLD fluctuations, and other distal causal mechanisms (e.g. a particular task stimulus that leaves respiratory fluctuations unaffected) may operate via the same intervening, proximal mechanisms. However, these findings have important implications for theories of the proximal cause of global BOLD fluctuations.

The proximate causal mechanism of global BOLD fluctuations is of great interest to fMRI researchers, due to its ubiquitous presence in spontaneous BOLD signals (Li et al., 2019; Liu et al., 2017; Power et al., 2017). It is helpful to separate the hemodynamic response to respiration and spontaneous global BOLD fluctuations into two phases: the early (~4s) overshoot phase of increased global BOLD signals, and the later (~14s) undershoot phase of decreased BOLD signals. It is unlikely that these phases correspond to the same causal mechanisms (Nakada et al., 2001). An often cited causal mechanism for the link between respiratory rate/depth and global BOLD fluctuations are respiratory-mediated changes in arterial CO2 concentration, a strong vasodilator (Chang & Glover, 2009; Wise et al., 2004). Decreases in arterial CO2 concentration is a causal candidate for the later undershoot phase, due to a presumed decrease in vasodilation (though sympathetic vasoconstriction effects may also represent a plausible causal candidate; see below).

The arterial CO2 explanation for global BOLD fluctuations is complicated by findings by ourselves and others that strong sympathetic nervous system activity is observed in response to voluntary respiratory volume changes (Häbler et al., 1994; Picchioni et al., 2022). A vasoconstrictive effect of sympathetic outflow to cerebral blood vessels is also consistent with the later undershoot phase. Cerebral blood vessels are profusely innervated by α-adrenergic receptors and may play a role in cerebral autoregulation (Koep et al., 2022), but the extent of their vasoconstrictive effect on cerebral blood vessels, and thereby BOLD signals in the brain, is controversial (van Lieshout & Secher, 2008). There is evidence that sympathetic regulation of cerebral blood flow may be most prominent at frequencies higher than 0.05Hz (Hamner et al., 2010), around the frequency range of co-fluctuations in respiratory volume and global BOLD fluctuations observed in this study. Assuming a sympathetic nervous system role, the transient increase in cerebral blood flow in the early overshoot of the hemodynamic response would activate a protective attenuation via sympathetic vasoconstriction to increased perfusion pressure.

Neither sympathetic vasoconstriction nor a decrease in arterial CO2 can explain the initial overshoot of the hemodynamic response (~4s) that corresponds to an early increase in global BOLD fluctuations. The transient increase in heart rate after inhalation observed in our respiration task analysis suggests a potential source of the early phase response, perhaps mediated by increases in arterial blood pressure (Panerai et al., 2000). However, the timing of the global BOLD peak is within the range of the time to peak (~4 - 6s) of the canonical

hemodynamic response to a brief stimulus impulse (Buxton et al., 2004). Consistent with local field potential and surface EEG studies in animal and human subjects (Ito et al., 2014; Kluger & Gross, 2021; Shams et al., 2021; Zelano et al., 2016), our study found an increase in broadband EEG power to respiratory volume fluctuations peaking at ~4s (**Figure 2**). However, the simultaneous timing of the early overshoot of the hemodynamic response with peaks of broadband EEG power suggests that these fluctuations are not a causal source of the early overshoot, given the conventional delay in neurovascular coupling (~4-6s). Nevertheless, the alignment of the early overshoot of the hemodynamic response to the canonical hemodynamic response and modulation of broadband EEG power, suggests that a neurogenic mechanism is one potential candidate for the early overshoot. A potential neurogenic mechanism may be mediated by noradrenergic brainstem nuclei (e.g. locus coeruleus) that project diffusely to the cortex (Samuels & Szabadi, 2008). Also relevant here is the growing literature in humans and rodents on the relationship between the respiratory cycle and oscillatory brain activity (Herrero et al., 2018; Ito et al., 2014; Karalis & Sirota, 2022; Kluger et al., 2021; Kluger & Gross, 2021; Zelano et al., 2016). These studies suggest that the respiratory cycle serves much more than a pulmonary gas exchange role, and may play a role in functional coordination of neuronal populations across the cortex (Heck et al., 2017). These respiration-mediated changes in oscillatory brain activity represent another potential neurogenic mechanism for the early overshoot phase of global BOLD fluctuations.

It is also important to distinguish between the standing and traveling wave components of global BOLD fluctuations (Bolt et al., 2022). The standing wave component of global BOLD fluctuations reflects simultaneous or zero-lag correlation, while the traveling wave component reflects time-lagged correlation. As described above, the traveling wave component of global BOLD fluctuations is characterized by a clear propagation towards large draining veins. This observation is consistent with a large-scale transit of oxygenated blood flow towards large cerebral vessels. However, similar propagation patterns are observed in electrocorticographic signals (Raut et al., 2021). Thus, the traveling wave component is likely to reflect a mixture of traveling cortical electric potentials and a cerebrovascular process. However, there is a prominent standing component in both the early undershoot and late overshoot phase of global BOLD fluctuations (Bolt et al., 2022) reflected by large amplitude BOLD increases in primary sensory/motor cortices, insular cortex and visual cortex. It is unclear whether these large amplitude increases in primary sensory and motor cortices are produced by neurovascular coupling, but they may reflect an independent mechanism than the traveling wave component.

These findings critically inform the global signal ‘noise’ vs ‘neural’ debate in the fMRI literature (Li et al., 2019; Liu et al., 2017; Murphy et al., 2009; Power et al., 2017; Uddin, 2017, 2020). Experimental identification of the proximal cause between respiratory volume fluctuations and global BOLD fluctuations will prove an important step in resolving this debate. While this paper takes no perspective on the removal of global fluctuations from resting-state fMRI recordings, it is clear that this spatiotemporal pattern of BOLD activity is linked with cognitively significant changes in peripheral physiology. In fact, similar physiological changes are observed in response to the presentation of a novel stimulus, facilitating reflexive orientation to the stimulus, known as the orienting reflex (Johnson & Lubin, 1967; Sokolov, 1963). Relatedly, it is

clear that global BOLD fluctuations are associated with EEG correlates of subcortical arousal, a clearly functional and ‘cognitive’ process. Our analysis of vigilance states and global BOLD fluctuations (**Figure 3**) found that global BOLD fluctuations are more prominent during states of low vigilance (i.e. drowsiness), consistent with previous findings (Falahpour et al., 2018; Soon et al., 2021; Wong et al., 2013). Further analysis suggested that global BOLD fluctuations and respiratory volume fluctuations are more strongly correlated during these low vigilance episodes. These findings suggest that the amplitude of global BOLD fluctuations (as well as CSF fluctuations) may serve as a potential biomarker of participant vigilance states (Gonzalez-Castillo et al., 2022).

Even assuming a purely cerebrovascular mechanism for global BOLD fluctuations, our findings make clear that these fluctuations are indirect measures of functionally significant physiological changes crucial to adaptive bodily function. An indirect measure of a functional neurophysiological process should not be readily dismissed as ‘noise’ or ‘artifacts’, as the BOLD contrast is fundamentally an indirect measure of neuronal activity. Further, the labeling of purely hemodynamic mechanisms as confounds in functional neuroimaging of cognitive function belies a neuron-centric view of information processing. Recent theories of neural information processing informed by discoveries in cell signaling pathways, propose a crucial role for hemodynamic processes in information processing (Moore & Cao, 2008; Pereira & Furlan, 2010). However, it is clear under some circumstances, such as fine-grained functional mapping of cortical organization, that large-scale fluctuation in BOLD signals would represent a confound to remove, regardless of its source. Thus, the appropriateness of attempts to remove it will likely be context dependent.

Supplementary Materials

Supplementary Movies

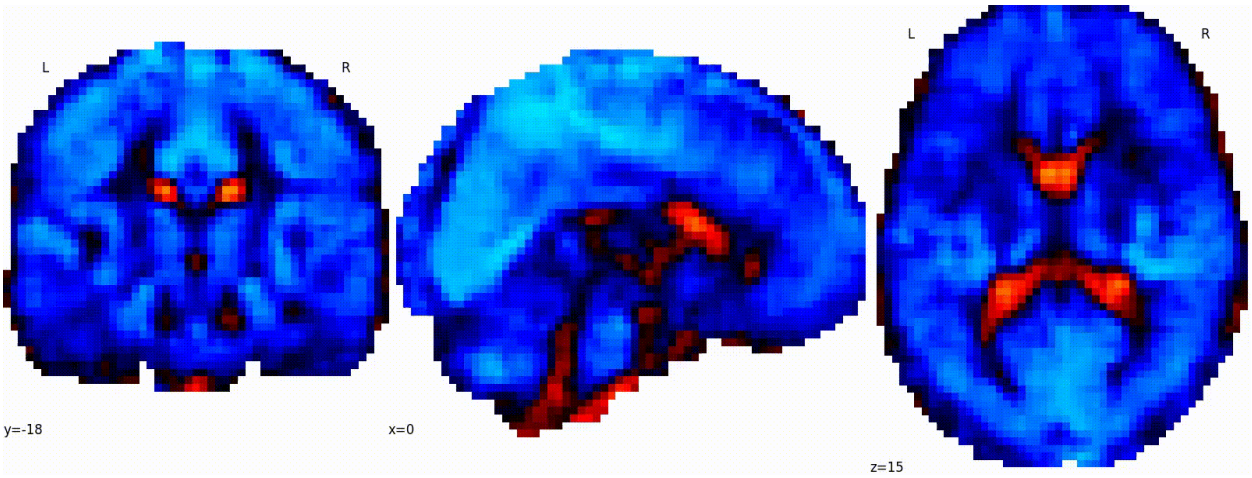

Supplementary Movie 1. **Temporal Reconstruction of Pattern One in ME-REST Dataset.**

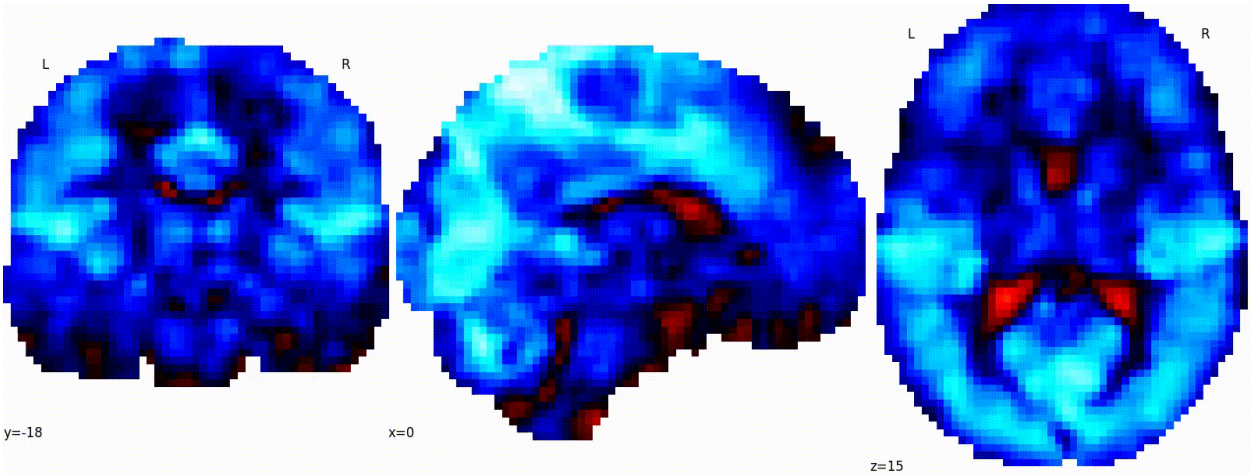

Supplementary Movie 2. **Temporal Reconstruction of Pattern One in HCP-REST Dataset.**

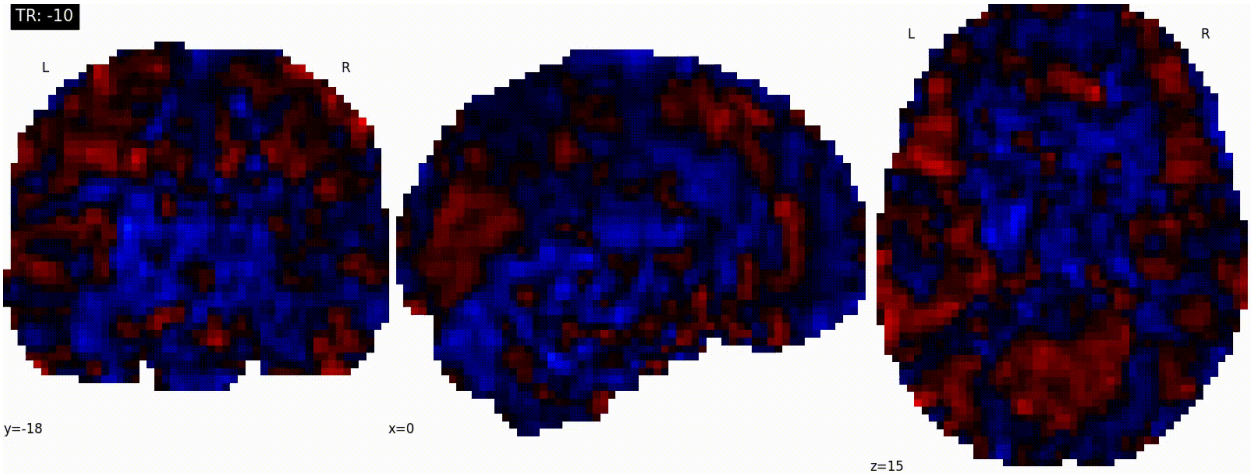

Supplementary Movie 3. **Peak Average High Respiratory Volume for ME-REST Dataset**.

Supplementary Tables

Dataset	Sample	Physio Signals	Source	Sample Size	Number of Sessions	Age Range	Sex (F)
ME-REST	Full	EEG, Respiration, PPG	Goodale et al. (2021). *ELife*. https://doi.org/10.7554/eLife.62376	11	15	21-35	6
ME-TASK	Full	EEG, Respiration, PPG	Unpublished dataset; https://www.cchanglab.net/	6	9	22-57	4
ME-REST-SUPP	Subset	Respiration, PPG	https://openneuro.org/datasets/ds003592/versions/1.0.11 **OpenNeuro Accession Number:** ds003592 **Version:** 1.0.11	42	42	20 - 34	20
HCP-REST	Subset	Respiration, PPG	https://www.humanconnectome.org/	30	30	22-37	17
NKI-TASK	Subset	Respiration, PPG, Skin Conductance	http://fcon_1000.projects.nitrc.org/indi/enhanced/	50	50	20-39	27
YALE-REST	Full	Pupillometry	https://openneuro.org/datasets/ds003673/versions/2.0.1 **OpenNeuro Accession Number:** ds003673	27	54	21 - 37	16

			Version: 2.0.1				

Supplementary Table 1. **Study Details and Demographics.**

Supplementary Figures

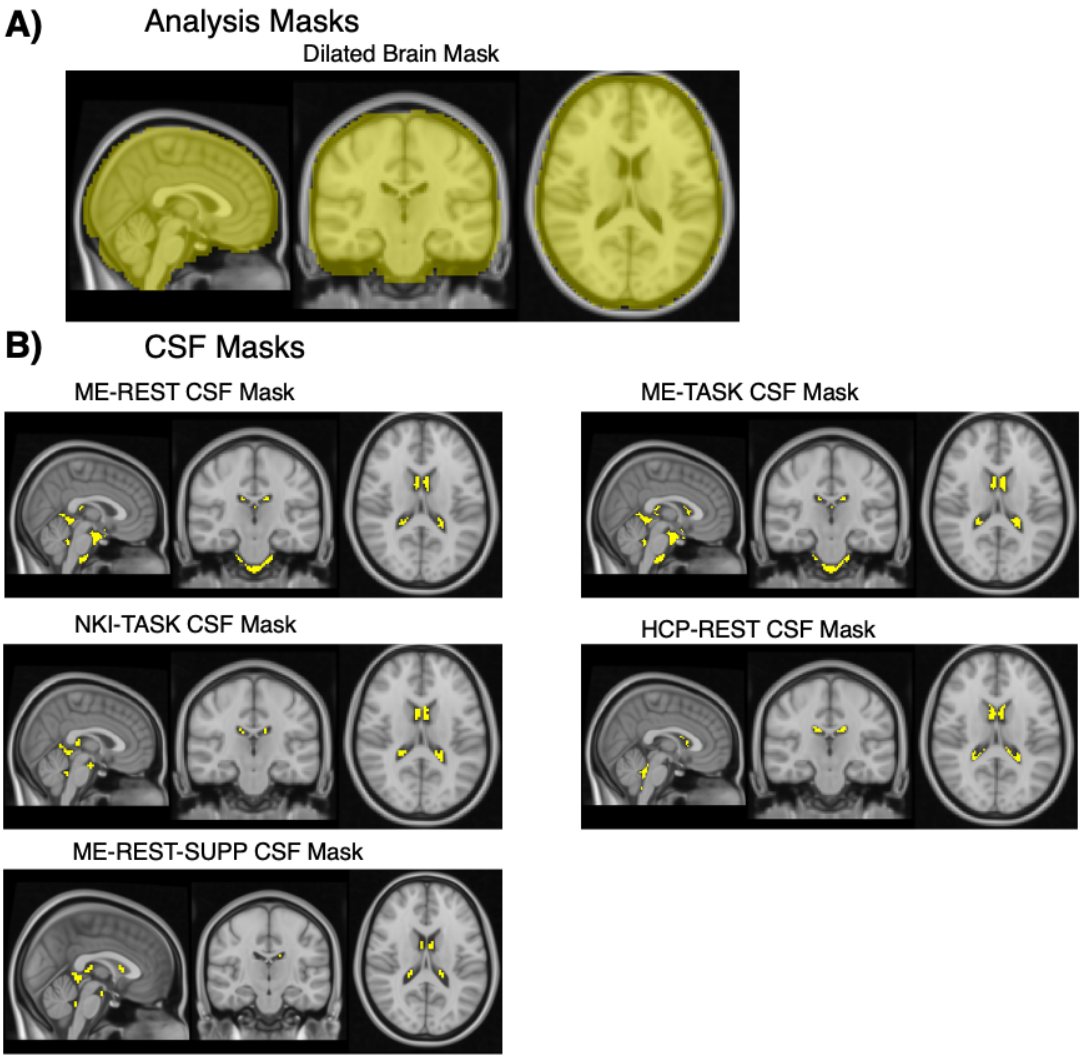

Supplementary Figure 1. **Analysis and Cerebrospinal Fluid Masks.** A) The dilated MNI (3mm) brain mask used to extract voxel time courses for analysis. The dilated mask was constructed from an MNI brain mask to pick up signals from draining veins and sinuses on the posterior and superior surfaces of the brain. B) The cerebrospinal fluid (CSF) masks used to extract averaged CSF BOLD signals for each dataset (see Methods).

ME-REST PPG Power Spectral Density

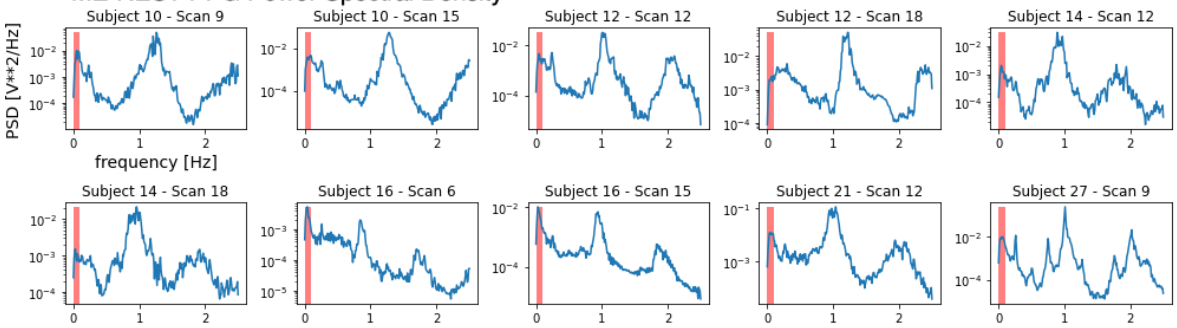

ME-Task PPG Power Spectral Density

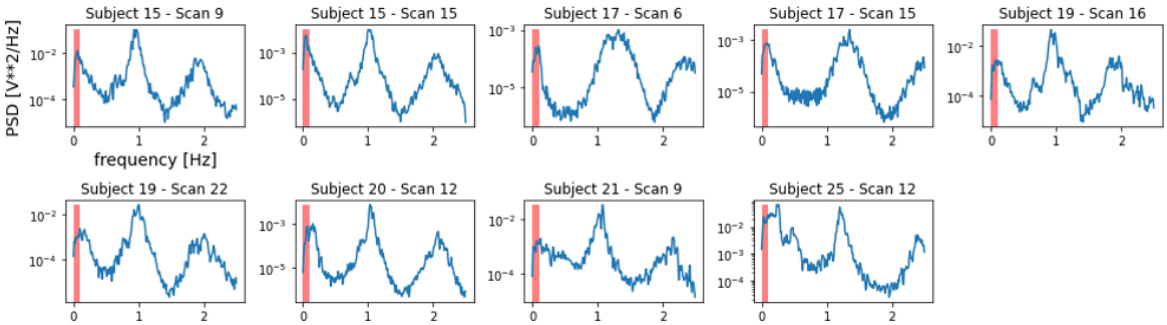

HCP-REST PPG Power Spectral Density

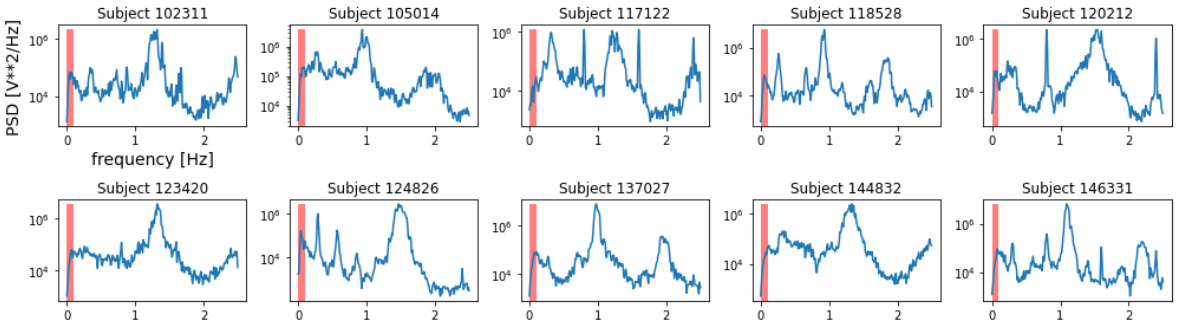

NKI-TASK PPG Power Spectral Density

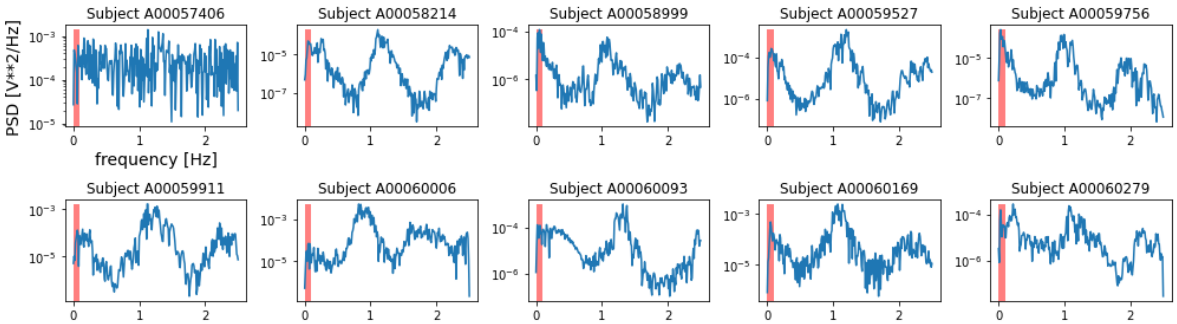

ME-REST-SUPP PPG Power Spectral Density

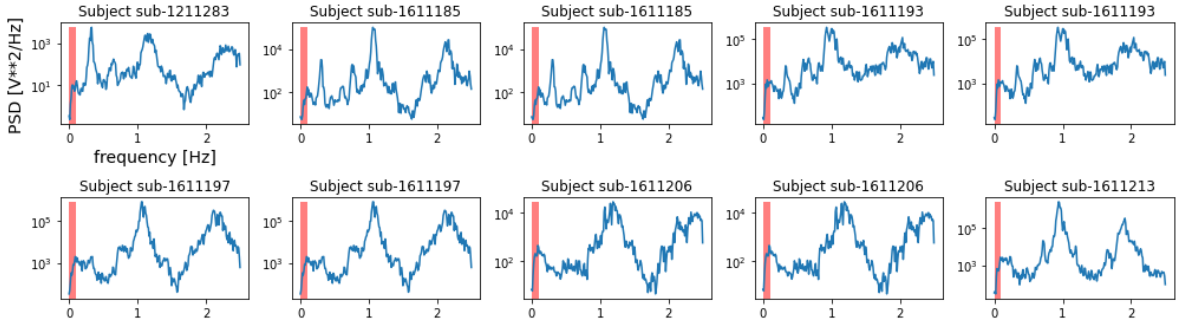

Supplementary Figure 2. **Power Spectral Density of Pulse Oximeter Time Courses Across Datasets.** Power spectral density estimates (0 to 2Hz) from pulse oximeter (PPG) signals displayed for the ME-REST, ME-TASK, HCP-REST, NKI-TASK and ME-REST-SUPP datasets. The power spectral density estimates are log-transformed on the y-axis. All PPG signals were resampled to a 5Hz sampling rate before power spectral density estimation. The power spectral density estimates were estimated using Welch's method (window length = 500 time points, window overlap= 50 time points).

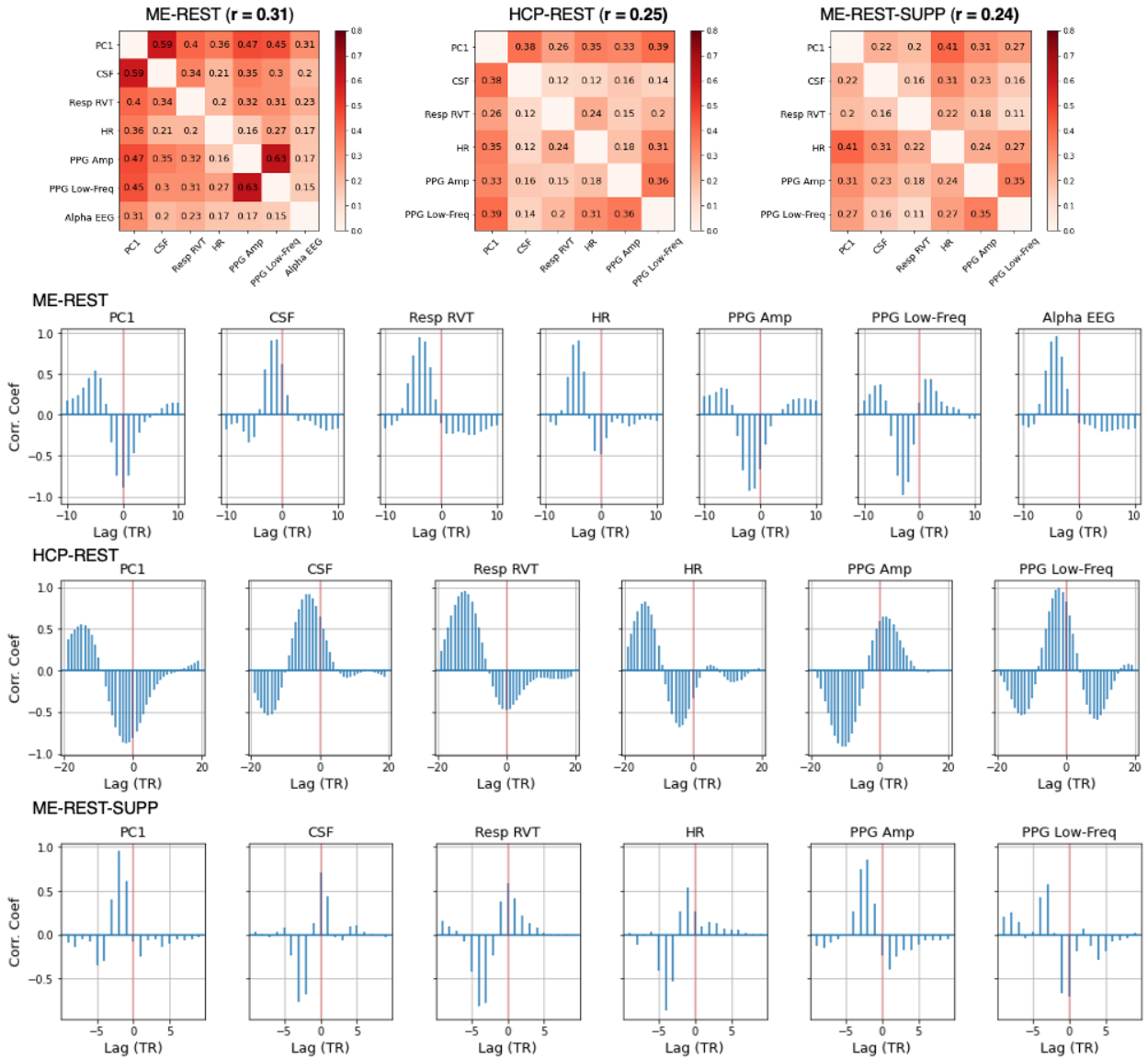

Supplementary Figure 3. **Multi-Set CCA Results Across Three Resting-State Datasets.** Mult-Set CCA results for the ME-REST, HCP-REST and ME-REST-SUPP datasets. The top panel displays the pairwise correlations between all electrophysiological signals (and PC1) in the first canonical component. The darker colors indicate stronger correlation. The average pairwise correlation for the first canonical

component is displayed above each correlation matrix. Note, there were differing electrophysiological signals per dataset. The bottom panel displays the cross-correlation between the original electrophysiological signal (group-wise temporally concatenated) and its canonical component time course for display of lead-lag relationships.

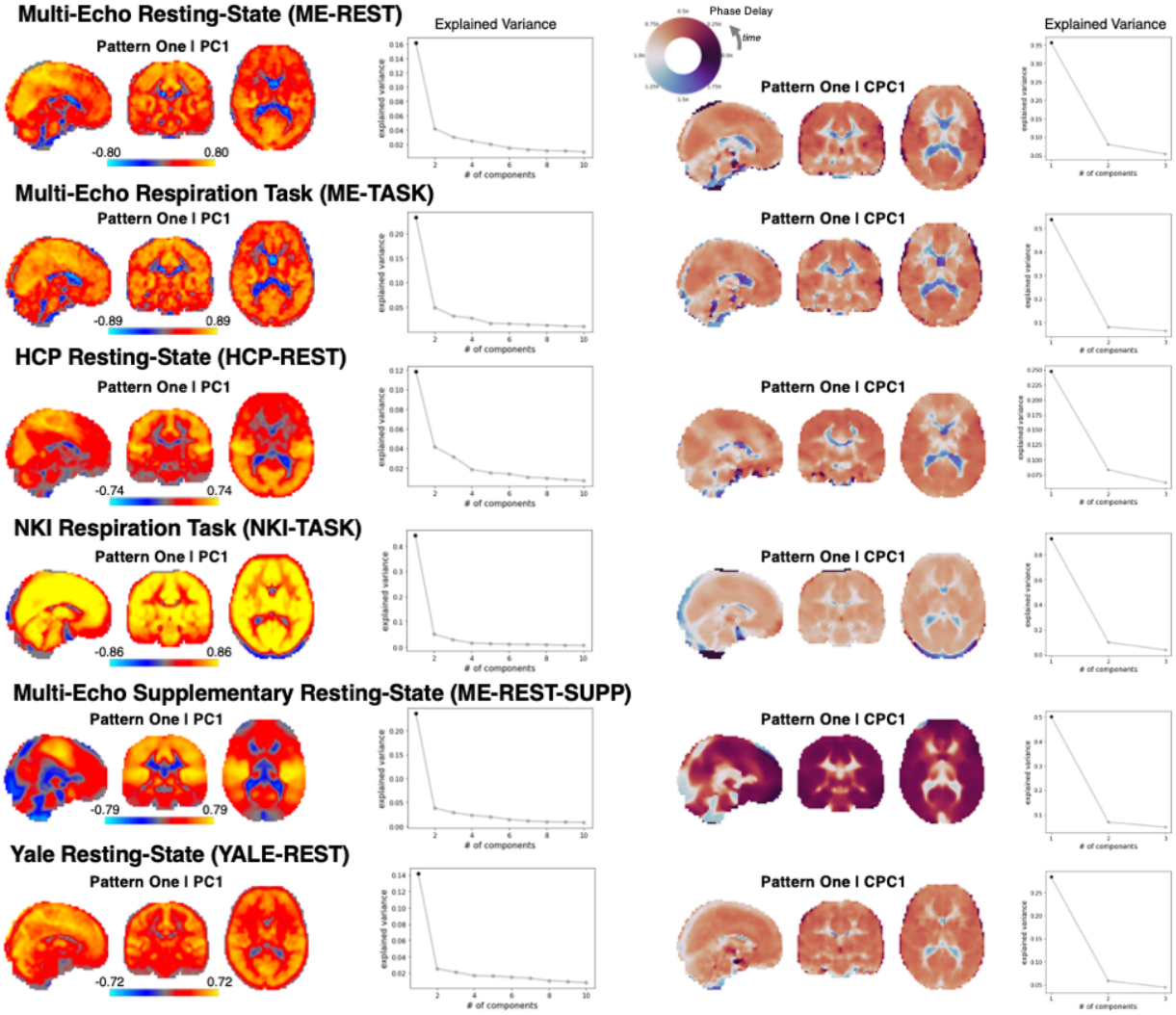

Supplementary Figure 4. **First Principal Component and Complex Principal Component Across Datasets.** Spatial weights of the first principal component (PC1; left) and phase delay maps of the first complex principal component (CPC1; right) across all datasets used in this study. Explained variance plots (Scree plots) are displayed to the right of each brain map displaying the explained variance by the first and subsequent principal components. The phase delay map of the first complex principal component encodes the time-delay (in radians) between voxels within the component. Because phase delay is measured in radians (0 to 2pi), they are displayed with a circular color map.

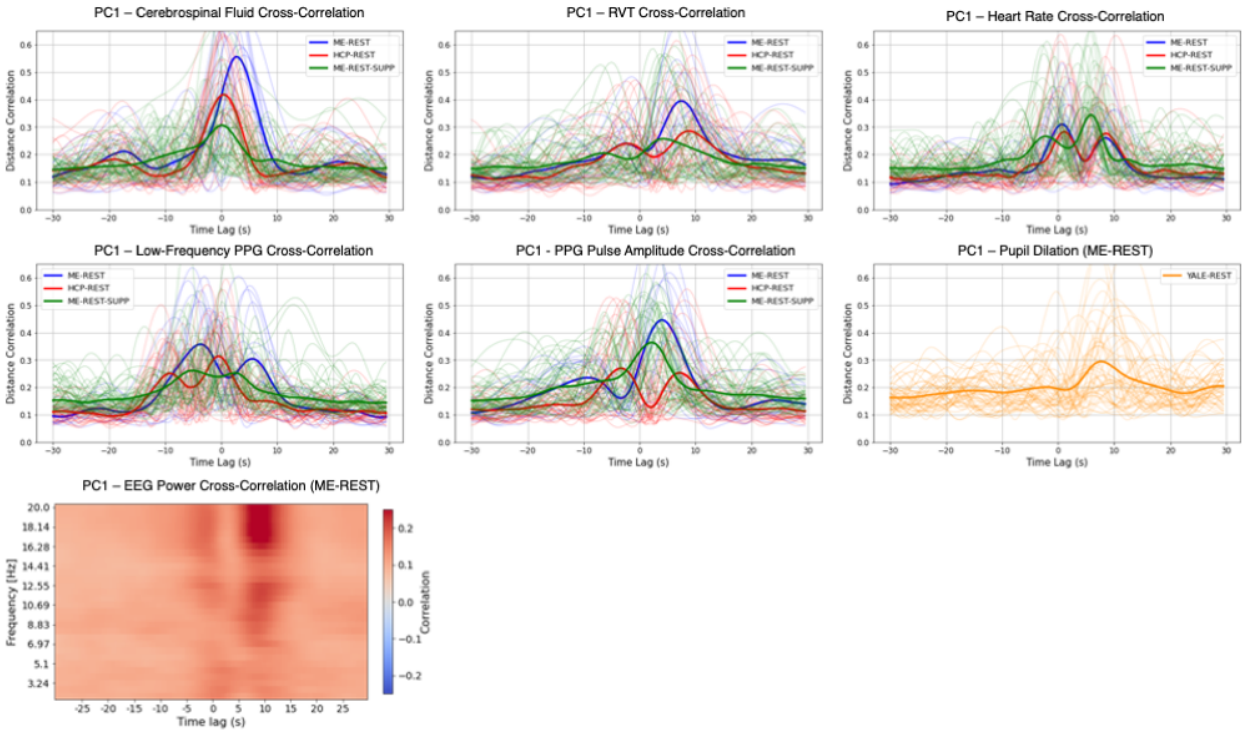

Supplementary Figure 5. **Cross-Distance Correlations Between Global BOLD and Physiological Time Courses.** To supplement the linear cross-correlation analyses in **Figure 2**, we analyzed potential non-linear associations between global BOLD (PC1) and electrophysiological time courses using distance correlation across time lags of the global BOLD time course. Distance correlation is a measure of statistical dependence (linear and nonlinear) between two vectors that varies between 0 (independence) to 1 (complete dependence). The cross-correlation plots simultaneously display results from ME-REST (blue), HCP-REST (red) and ME-REST-SUPP (green) datasets. All subject-level cross-correlations are displayed in lighter, more transparent color, while the mean signal across subjects is displayed in a darker color.

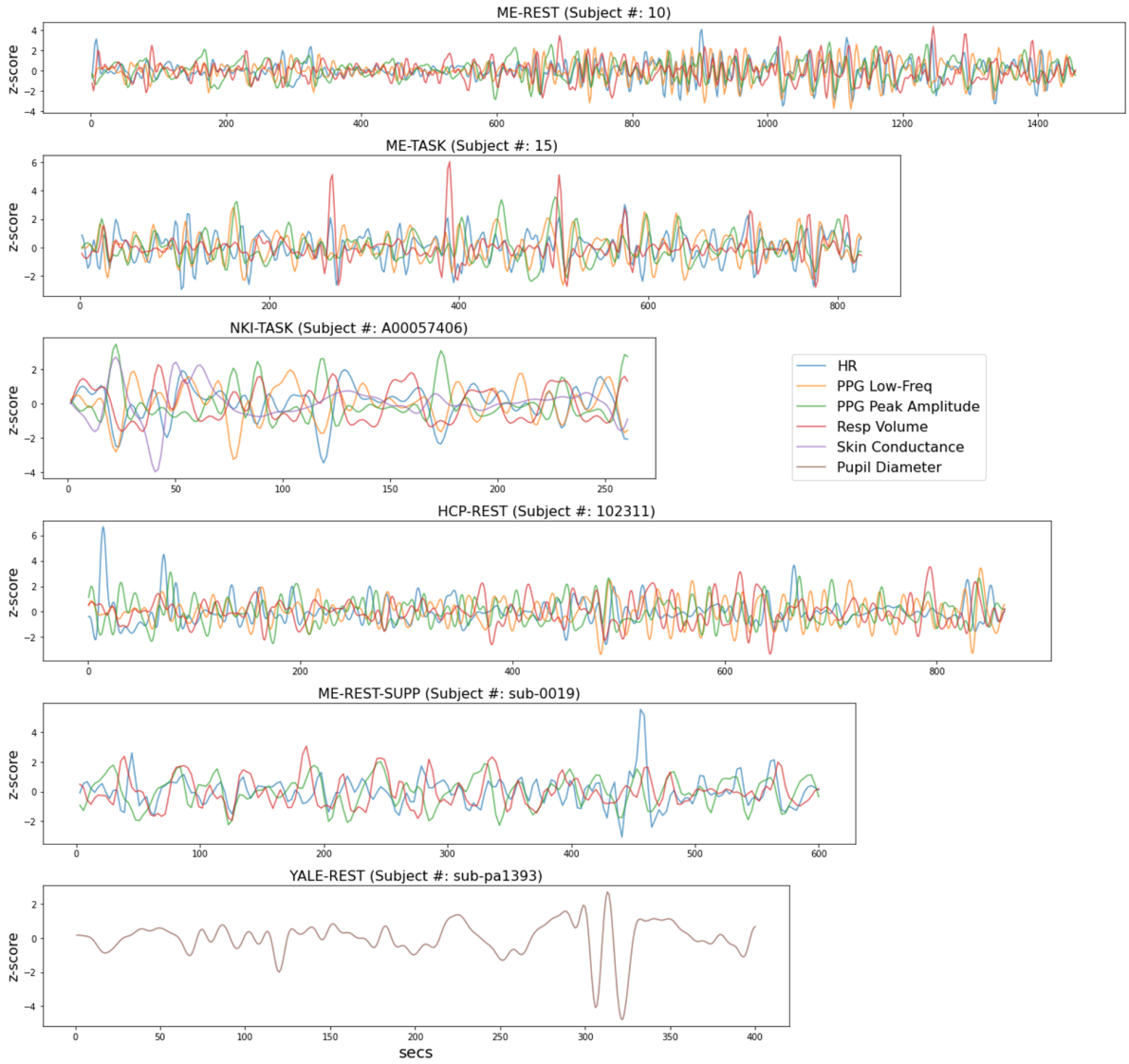

Supplementary Figure 6. **Physiological Time Series from Example Subjects.**

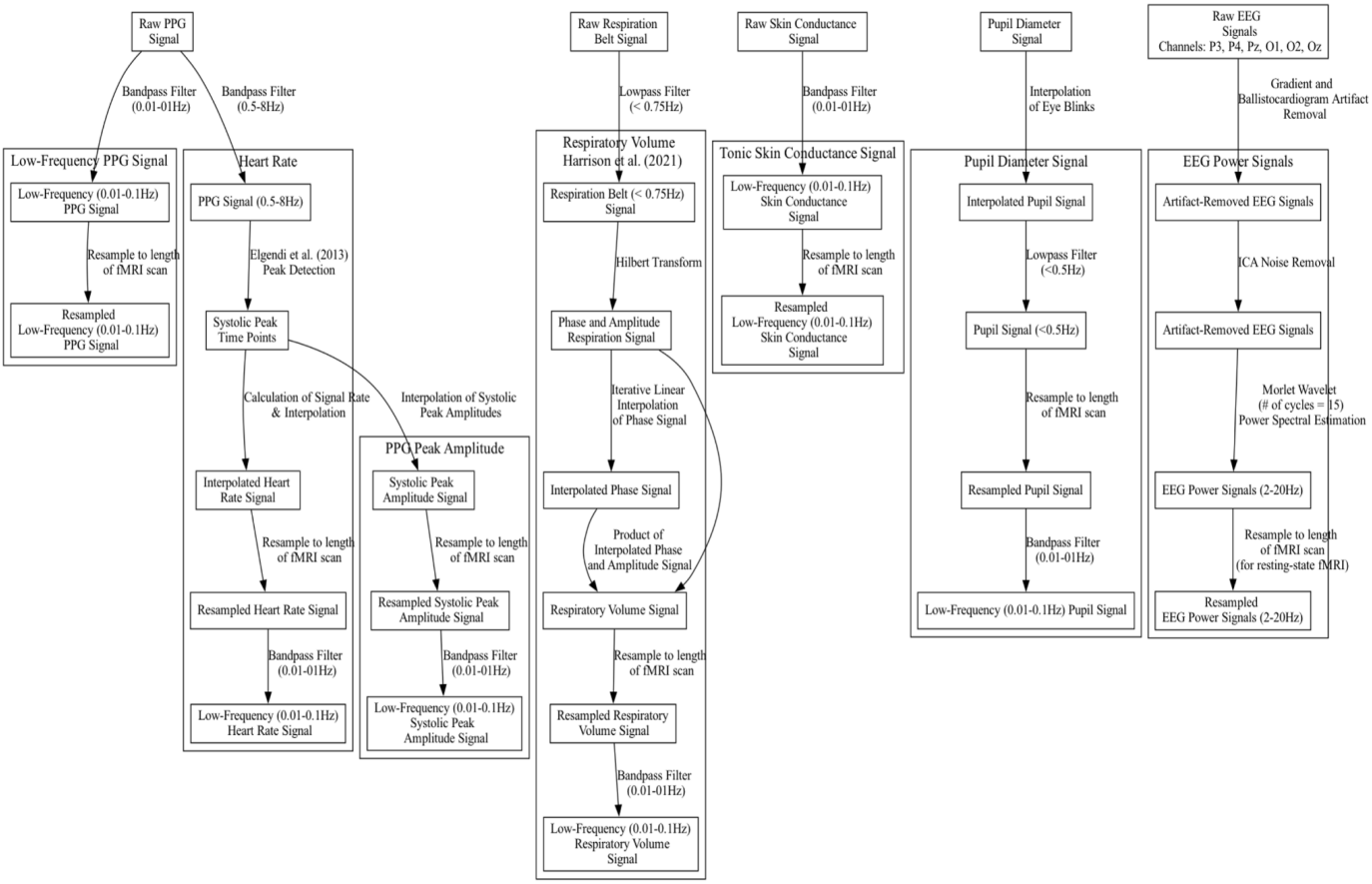

Supplementary Figure 7. **Electrophysiological Signal Preprocessing Pipeline.**

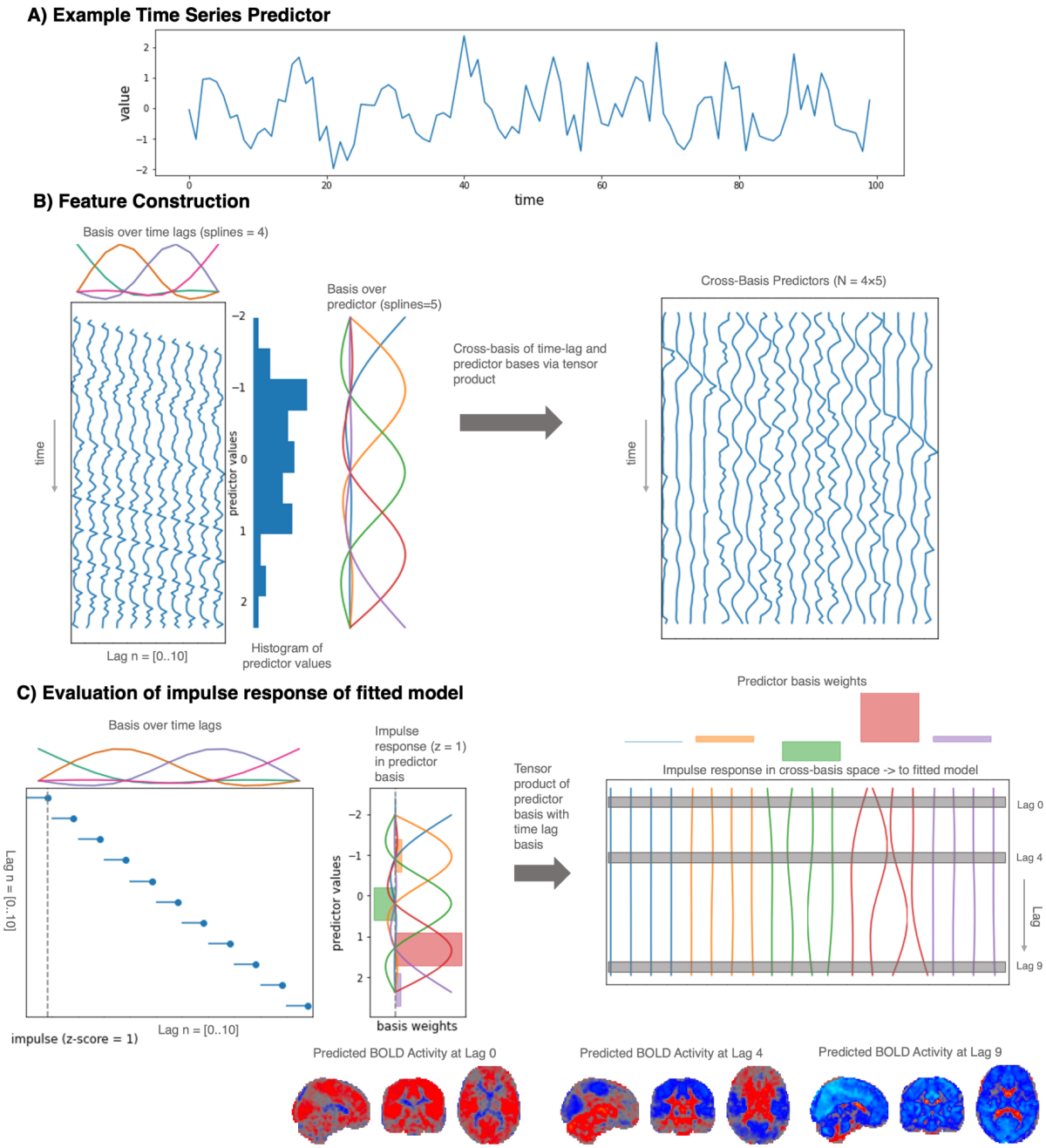

Supplementary Figure 8. **Illustration of Feature Construction and Model Evaluation in Distributed Lag Nonlinear Model.**

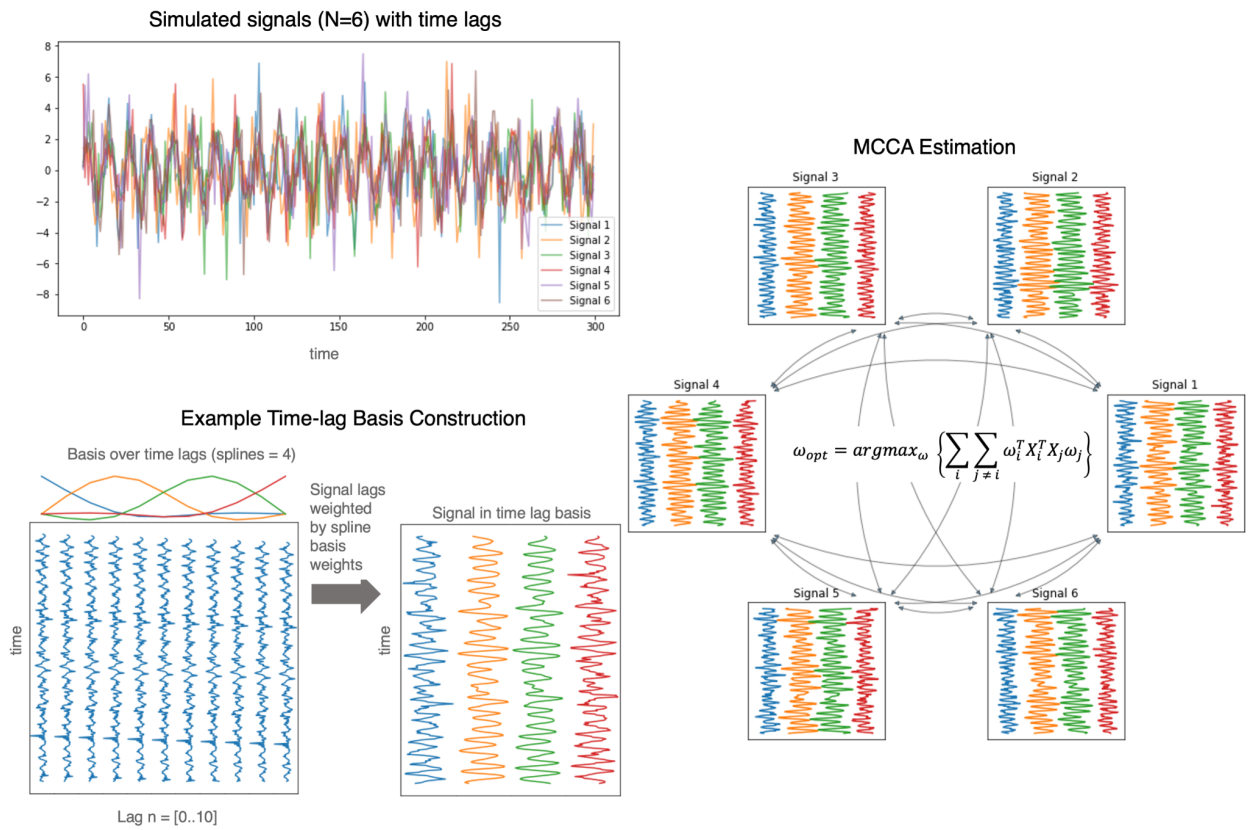

Supplementary Figure 9. **Illustration of Multiset Canonical Correlation Analysis.**

Methods and Materials

Participants and Data Acquisition

Six datasets were analyzed in this study: 1) a simultaneous EEG/multi-echo resting-state fMRI dataset (ME-REST), 2) a simultaneous EEG/multi-echo respiration task fMRI dataset (ME-TASK), 3) a multiband accelerated single-echo resting-state fMRI dataset from the Human Connectome Project (Van Essen et al., 2013) (HCP-REST) , 4) a multiband accelerated single-echo fMRI respiration task with simultaneous physiological recordings from the enhanced Nathan Kline Institute (NKI) - Rockland Sample (Nooner et al., 2012) (NKI-TASK), 5) a supplementary multi-echo fMRI resting-state dataset with simultaneous physiological recordings (Spreng et al., 2022) (ME-REST-SUPP), and 6) a multiband accelerated single-echo resting-state fMRI dataset with simultaneous pupillometry from Yale University (Lee et al., 2022) (YALE-REST). Dataset details and demographics are presented in **Supplementary Table 1**.

ME-REST and ME-TASK Data

Simultaneous multi-echo fMRI-EEG eyes-closed resting-state scans (ME-REST) were acquired from 11 healthy, right-handed participants (6 females, mean age = 25.9). All subjects provided written informed consent, and human subjects protocols were approved by the Institutional Review Boards of the National Institutes of Health and Vanderbilt University. Two resting-state sessions were recorded for four of the subjects, creating a total of 15 scans. Simultaneous multi-echo fMRI-EEG respiration task scans (ME-TASK) were acquired under the same acquisition protocol for six healthy, right-handed participants (4 females, mean age = 30.5). Two task sessions were recorded for three of the subjects, creating a total of 9 scans. The respiration task experimental design consisted of a sparse event-related design with instructions to the participants to take a deep breath in response to an auditory cue (a constant tone). The timing between auditory cue onset was randomly jittered between the range of 60.55 and 131.25 sec. Auditory cue timing was consistent across scans. One participant overlapped between the resting-state and respiration task sessions.

Detailed MRI/EEG acquisition parameters are provided in Goodale et al. (2021). Briefly, anatomical T1-weighted structural and multi-echo EPI BOLD scans were collected on a 3T Siemens Prisma scanner with a Siemens 64-channel head/neck coil. The multi-echo EPI sequence was acquired with TR = 2100 ms, echo times = 13.0, 29.4, and 45.7 ms, flip angle = 75 degrees, and voxel size = 3mm isotropic. The duration of the resting-state scan was 24.5 minutes, corresponding to a total of 700 volumes. The duration of the respiration task scan was slightly variable (14-15 minutes across subjects), corresponding to a total of 400-435 volumes, depending on the subject. Simultaneous scalp EEG (sampling rate = 5 kHz) was acquired during the resting-state and respiration task using a 32-channel MR-compatible system. The scalp EEG channel time courses were referenced to channel FCz. Photoplethysmography (PPG) and respiration belt signals (sampling rate: 2 kHz) were acquired during both the resting-state and respiration task sessions. The PPG transducer was placed on the left index finger.

MRI scan triggers were recorded along with EEG and physiological signals for data synchronization.

HCP-REST Data

We analyzed eyes-open resting-state fMRI EPI scans from the HCP S1200 release. We randomly selected 30 unrelated, healthy young adults (ages 22–37; 17 females) for our study with high quality physiological recordings (confirmed through visual inspection). We chose 30 subjects for two reasons: 1) analyses were found to be replicable at small sample sizes (< 15 subjects) for the HCP dataset, and 2) the length of the scans (length of scan: 1200 time points) imposed significant computational challenges (> 80GB RAM). Detailed MRI/Physio acquisition parameters are provided in Smith et al. (2013). Briefly, resting-state fMRI scans were collected on Siemens 3T Tim Trio scanners with a multiband (factor of 8) accelerated EPI sequence with the following parameters: TR: 720ms, TE = 33.1ms, flip angle = 52 degrees, and voxel size= 2mm isotropic. Resting-state fMRI data was collected over two consecutive days for each subject and two sessions, each consisting of two 15-minute runs, amounting to four resting-state sessions per subject. Within a session, the two runs were acquired with opposite phase encoding directions: L/R encoding and R/L encoding. A single 15 min scan from each participant on the first day of scanning was selected. We balanced the number of L/R and R/L phase encoding scans across our participants (n=15 for L/R direction) to ensure results were not biased by acquisition from any given phase encoding direction. Photoplethysmography (PPG) and respiration belt signals (sampling rate = 400 Hz) were simultaneously acquired with resting-state EPI scans along with MRI scan triggers for data synchronization.

NKI-TASK Data

We analyzed task-fMRI breath-hold EPI scans and high-resolution anatomical T1w images from the enhanced Nathan Kline Institute (NKI) Rockland sample. We randomly selected 50 adult subjects for our analysis (ages 20-39, 27 females). A single respiration task session was recorded per participant. The respiration task scan was collected as part of a longer scanning session acquiring multiple functional scans per participant. Detailed acquisition parameters are provided on the Enhanced NKI-Rockland webpage (http://fcon_1000.projects.nitrc.org/indi/enhanced/index.html). Briefly, breath hold fMRI scans were collected on a Siemens 3T Tim Trio scanner with a multiband (factor of 4) accelerated EPI sequence with the following parameters: TR = 1400ms, TE = 30ms, flip angle = 65 degrees, voxel size = 2mm isotropic. The respiration task was a block design with the following sequence: 1) a 10-sec rest, 2) a 2-sec visual stimulus indicating the start of the trial (text: ‘Get Ready’), 3) a 2-sec inspiration, 4) a 2-sec expiration, 5) a 2-sec deep inspiration, and 5) a breath hold for 15-sec. This sequence was repeated seven times, for a total duration of 4.5 minutes. PPG signals (recorded from the tip of the index finger), skin conductance (galvanic skin response; recorded from the hand), and respiration belt signals were simultaneously acquired with task-fMRI EPI scans along with MRI scan triggers for data synchronization.

ME-REST-SUPP Data: Replication analysis

As a supplementary multi-echo fMRI dataset to confirm findings from the ME-REST and HCP-REST datasets, we analyzed eyes-open resting-state data from the neurocognitive aging data release (Spreng et al., 2022) via OpenNeuro (Markiewicz et al., 2021; OpenNeuro Accession Number: ds003592). We selected 87 young adults with high quality physiological recordings (confirmed through visual inspection) (ages 20 - 34, 20 females). Each participant performed two resting state fMRI sessions during the study visit. Detailed MRI acquisition parameters are provided in Spreng et al. (2022). Briefly, anatomical T1-weighted structural and multi-echo EPI BOLD-fMRI scans were collected on a 3T GE Discovery MR750 scanner with a 32-channel head coil. The multi-echo EPI sequence was acquired with TR = 3000 ms, echo times = 13.7, 30, and 47 ms, flip angle = 83 degrees, and voxel size = 3mm isotropic. The duration of the resting-state scan was 10 minutes, corresponding to a total of 204 volumes. Photoplethysmography (PPG) and respiration belt signals (sampling rate: 40 or 50 Hz) were acquired during the session.

YALE-REST Dataset

For analysis of pupillometry signals, we analyzed eyes-open resting-state fMRI data from the Yale Resting-State Pupillometry/fMRI dataset (Lee et al., 2022) via OpenNeuro (Markiewicz et al., 2021; OpenNeuro Accession Number: ds003673). All 27 participants were selected for analysis (ages 21 - 37, 16 females). Both resting-state fMRI sessions collected during the study visit were used. Detailed MRI acquisition parameters are provided in Markiewicz et al. (2021). Briefly, anatomical T1-weighted structural and single-echo, multiband EPI BOLD-fMRI scans were collected on a MAGNETOM Prisma MRI scanner. The single-echo, multiband EPI sequence was acquired with TR = 1000ms, TE = 30ms, multiband acceleration factor = 5, flip angle = 55 degrees and voxel size = 2mm. The duration of the resting-state scan was 6 minutes and 50s. Simultaneous eye-tracking was recorded using a MR-compatible infrared EyeLink 1000 Plus eye-tracking system with a 1000Hz sampling rate. A centroid fitting model from the EyeLink system was used for pupil tracking. We used minimally preprocessed pupil data provided by the authors for analysis (see details below).

MRI Data Preprocessing

For all but the HCP-REST dataset, datasets were downloaded in raw (unprocessed) NIFTI formats. Depending on the nature of the EPI-BOLD acquisition, the five datasets were processed with slightly different preprocessing pipelines. We first describe dataset-specific preprocessing, and then describe common preprocessing stages that were applied to all datasets.

For the ME-REST and ME-TASK datasets, more comprehensive preprocessing details are provided in Goodale et al. (2021). Briefly, the ME-REST and ME-TASK EPI-BOLD preprocessing pipelines consisted of the following steps: the first 7 volumes were removed, six-parameter rigid body motion correction and slice timing correction with *3dvolreg* and *3dTshift* in

AFNI (https://afni.nimh.nih.gov/), Multi-Echo ICA denoising using Tedana software (DuPre et al., 2020), non-linear registration to the MNI152 template using SPM software (https://www.fil.ion.ucl.ac.uk/spm/), removal of spikes (outliers) from the time courses using 3dDespike in AFNI, and spatial smoothing with a gaussian kernel (FWHM=3mm) in AFNI.

For the HCP-REST dataset, we used EPI-BOLD scans previously preprocessed with the HCP's ICA-based artifact removal process (Smith et al., 2013) to minimize effects of spatially structured noise in our analysis. Analysis of the minimally-preprocessed EPI scans without ICA-based artifact correction (and run through the common dataset preprocessing stages described below) yielded similar findings. EPI scans were previously motion-corrected, registered to the MNI152 template, and intensity normalized. Comprehensive details of the HCP preprocessing pipeline are described in Glasser et al. (2013) .

For the NKI-TASK and YALE-REST dataset, the EPI-BOLD scans were first motion corrected with six-parameter rigid body alignment with FSL MCFLIRT, and then non-linearly registered to the MNI152 template using FSLs FMRIB's Non-Linear Image Registration Tool (FNIRT) (Andersson et al., 2010).

For the ME-REST-SUPP dataset, the first echo EPI-BOLD scan was subjected to motion correction with six parameter rigid body alignment implemented in FSL MCFLIRT, and the motion alignment parameters were applied to the second and third echo scans. Slice timing correction was then applied to each EPI-BOLD echo using FSL's slicetimer utility. As with the ME-REST and ME-TASK datasets, multi-echo ICA denoising and optimal combination of echos was performed using Tedana software (DuPre et al., 2020). The first 4 volumes of the scan were discarded, and then non-linear registration to the MNI152 template was applied using FNIRT.

For the ME-REST-SUPP dataset, brain extraction of anatomical images was carried out with FSL BET and the first 4 functional volumes were discarded. Anatomical and functional images were then submitted to Multi-Echo ICA as implemented in AFNI (Kundu et al., 2013, 2014), which first performs slice-timing correction, de-obliquing, and rigid body motion correction with six parameters prior to optimally combining the TEs and denoising. Further detail on preprocessing and denoising is provided in Setton & Mwilambwe-Tshilobo et al (2023).

Following dataset-specific preprocessing, all datasets were then resampled to 3mm (isotropic) MNI152 space, spatially smoothed with a gaussian kernel (FWHM=5mm) using FSL and temporally filtered with a fifth-order Butterworth bandpass zero-phase filter (0.01-0.1Hz). For all datasets, voxels were extracted with a dilated MNI152 brain mask, so as to pick up voxel time courses in large dural venous sinuses and CSF compartments (**Supplementary Figure 1**).

Physiological and EEG Feature Extraction

Six physiological signals were extracted from the raw PPG, respiration belt, skin conductance, and pupil diameter recordings. Heart rate variability, systolic peak amplitude (PPG

pulse amplitude) and low-frequency (0.01-0.1Hz) PPG signals were extracted from raw PPG recordings. Respiratory volume (Harrison et al., 2021) was extracted from the raw respiration belt recordings. Low-frequency (0.01-0.1Hz) tonic skin conductance was extracted from the raw skin conductance signals. We used minimally-preprocessed pupil diameter signals extracted from eye-tracking recordings provided by the authors (Lee et al., 2022). For comparison with BOLD fMRI signals, the extracted physiological signals were clipped at five standard deviations from the mean (for outlier removal), resampled to the length of the functional MRI scan and filtered using a fifth-order Butterworth bandpass filter (0.01-0.1Hz) excluding the low-frequency PPG and tonic skin conductance signals that were already filtered. Note: the minimally-preprocessed pupil diameter signals were already resampled to the length of the functional scan. Details of the preprocessing for each physiological signal are provided below. The preprocessing pipeline for the physiological signals (and EEG signals) is illustrated in **Supplementary Figure 7.**

Heart rate variability time courses were extracted from PPG time courses using the NeuroKit2 package (https://neuropsychology.github.io/NeuroKit/index.html) in Python. For calculation of HR, the raw PPG time course was first filtered with a third-order Butterworth bandpass filter (0.5 - 8Hz) followed by systolic peak detection using the method by Elgendi et al. (2013). Heart rate was calculated from the period of time between peaks and interpolated to the same length of the raw signal with monotone cubic interpolation (Fritsch & Butland, 1984). For extraction of PPG pulse amplitude signals, the amplitude of the systolic peaks (previously identified by the peak detection method) were interpolated with monotone cubic interpolation.

Work by Tong et al. (2012) found that widespread brain hemodynamics were correlated with low-frequency (0.01 - 0.1Hz) oxygenation signals in the periphery measured by near-infrared spectroscopy (NIRS). We assessed whether a similar peripheral low-frequency oxygenation signal was present in the PPG time courses recorded during the ME-REST and ME-TASK datasets. Inspection of the power spectral density estimates of the PPG time courses revealed a detectable, low-frequency signal in the 0.01 - 0.1 Hz range (**Supplementary Figure 2**). For the comparison of this signal with BOLD time courses, we filtered the PPG time courses with a fifth-order Butterworth bandpass filter (0.01-0.1Hz). Low-frequency PPG signals were attenuated in the HCP-REST and ME-REST-SUPP dataset, though detectable (**Supplementary Figure 2**).

For the NKI-TASK dataset, skin conductance (SC) signals were collected from the hand. SC time courses consist of a low-frequency tonic and high-frequency phasic component (Lykken & Venables, 1971). The tonic component reflects the slowly-varying component of the skin conductance signal, and has previously been studied in the context of fMRI (Nagai et al., 2004). We extracted a narrowband tonic SC signal matching the frequency content of spontaneous resting-state BOLD signals (0.01-0.1Hz) with a fifth-order Butterworth bandpass filter (0.01-0.1Hz).

For the YALE-REST dataset, we used minimally preprocessed pupillometry signals provided by the authors (https://openneuro.org/datasets/ds003673/versions/2.0.1). The minimal

preprocessing pipeline consisted of 4-point spline interpolation of eye blinks, low-pass filtering with a Butterworth filter (< 0.5 Hz), removal of the first 10 seconds of recordings (to match the length of the functional scan), and resampling to the sampling frequency of the functional scan (1 Hz).

Respiratory volume (RV) was calculated from respiration belt time courses using a recently developed Hilbert-based method (Harrison et al., 2021), implemented in NeuroKit2. High-frequency noise was first removed from the respiratory belt time courses with a Butterworth tenth-order low-pass filter (< 0.75Hz). Amplitude and phase components were then extracted from the filtered signal via the Hilbert Transform. Following an iterated linear interpolation procedure of the phase time courses, RV was calculated as the product of the derivative of the interpolated phase time course (i.e. the instantaneous breathing rate) with the signal amplitude (breathing depth/amplitude). For the analyses presented in **Figure 2**, these two components of the RV, the breathing depth/amplitude and instantaneous breathing rate, were analyzed separately.

For simultaneously-collected EEG data in the ME-REST and ME-TASK datasets, channel time courses were first corrected for gradient artifacts through the average artifact subtraction method (Allen et al., 2000). Ballistocardiogram artifacts were removed by subtraction of an average artifact template locked to cardiac R-peaks, followed by independent component analysis (ICA) of the template-subtracted time courses. These EEG preprocessing steps were performed with the BrainVision Analyzer software. EEG power and vigilance fluctuations were extracted from averaged parietal and occipital lobe EEG channel time courses (P3, P4, Pz, O1, O2, Oz) using the MNE-Python package (Gramfort et al., 2013) (https://mne.tools/stable/index.html). Time-frequency EEG power was extracted via Morlet wavelet filters (number of cycles = 15) to construct a filter bank ranging from 2 to 20Hz (spanning Delta, Theta and Alpha oscillation bands). For the ME-REST dataset, power was extracted from each signal in the filter bank and was cross-correlated with time courses from the first principal component of the fMRI data (see below). Alpha amplitude signals were computed through band-pass FIR filtering (Hamming window; 8 - 12Hz) of the average channel time course, followed by extraction of instantaneous amplitude via the Hilbert Transform. Vigilance time courses were extracted from the ratio of alpha and theta root mean square amplitude signals extracted via a rolling window of 2s. As our interest was in low-frequency vigilance state changes across the course of the scanning session, we applied a low-pass fifth-order Butterworth filter (< 0.01 Hz). For comparison with fMRI time courses in the ME-REST dataset, EEG power and vigilance signals were resampled to the length of the fMRI scan.

CSF Extraction

For the ME-REST, ME-TASK and NKI-TASK datasets, CSF signals were extracted from tissue segmentation masks of the high-resolution anatomical T1w images using FSL's FMRIB's Automated Segmentation Tool (FAST) (Zhang et al., 2001). Subject-level CSF masks were created by thresholding (p > 0.9) CSF partial volume images, representing the portion of CSF at each voxel. For group analysis, subject-level masks were registered to the MNI152 space using

the subject's FNIRT transformation parameters derived from the T1w to MNI152 non-linear registration. Group-level CSF masks were constructed by thresholding the summed binarized subject-level CSF masks within each dataset. The threshold (# subject overlap) that was used to extract group-level masks was determined by visual inspection; ME-REST - 10 subjects (out of 11); ME-TASK - 4 (out of 8); NKI-TASK - 40 (out of 50), ME-REST-SUPP - 70 (out of 87), YALE-REST - 25 (out of 27). To ensure that only CSF signal within the ventricles was included, we removed voxels from the group-level CSF masks that did not overlap with FSL's MNI152 ventricle mask.

For the HCP-REST dataset, CSF signals were extracted from subject-level Freesurfer anatomical parcellations in MNI space output from the HCP minimal-preprocessing pipeline (Glasser et al., 2013) as in Gonzalez-Castillo et al., 2022. Lateral and fourth ventricle masks were combined to create a ventricle mask per subject. Group-level CSF masks were extracted from the overlap of subject-level CSF masks in the same manner above: 28 subjects (out of 30).

Principal Component Analysis

As in Bolt et al. (2022), the zero-lag and time-lag structure of the global BOLD signal was modeled with principal component analysis (PCA) and complex principal component analysis (CPCA), respectively. As shown in Bolt et al. (2022), the first principal component of both PCA and CPCA extract a pattern of global BOLD fluctuations that is closely correlated (in time) with the global mean time course. Standard PCA was used to extract the simultaneous statistical dependence between cortical areas of global BOLD fluctuations, CPCA was used to extract time-lag statistical dependence (i.e. traveling wave or propagatory behavior). In this study, we analyze the properties of the first principal component in volume space, including signals from subcortical structures, ventricles and cerebral sinuses.

CPCA involves the application of PCA to complex-valued time courses generated by the Hilbert transform. We extracted the first complex principal component using CPCA on the complex-valued (bandpassed to 0.01-0.1Hz) BOLD time courses temporally-concatenated across subjects. Time-lag information can be extracted from the phase representation of the complex-valued PC (via Euler's Identity). The phase representation encodes the time-delay between voxels (in radians) within the first complex PC. The time-lag information can also be visualized over selected time points via a temporal reconstruction. Comprehensive details are provided in Bolt et al. (2022). Briefly, we first divided the temporal phase time courses of the first complex PC into equally-spaced bins (N=30). We then projected the complex PC back into voxel space to derive voxel time courses. Finally, we averaged the real-valued voxel time courses within the time points indexed by the equally-spaced phase bins. This resulted in a 30-volume 'movie' that visualizes the temporal evolution of a component. Both PCA and CPCA solutions were computed using a fast randomized SVD algorithm developed by *Facebook* (https://github.com/facebookarchive/fbpca). More details of the CPCA algorithm can be found in Bolt et al. (2022).

Cross-Correlation Analyses

For the ME-REST, HCP-REST, ME-REST-SUPP and YALE-REST datasets, cross-correlation analyses were conducted between the electrophysiological time courses and the first principal component (PC1) time course. Product-moment cross-correlations were computed at the subject-level and group-average cross-correlations were computed by the mean of the subject-level cross-correlations. For comparability across datasets with different sampling rates, we interpolated subject and group-average cross-correlation functions with a cubic spline from -30s to 30s (time-lag).

Product-moment correlations quantify linear dependence between electrophysiological time courses and the principal component time course. To examine potential nonlinear dependencies, we computed cross-correlations between time courses using distance correlation (Székely et al., 2007), a measure of statistical dependence (linear and nonlinear) between two vectors that varies between 0 (independence) to 1 (complete dependence). Distance correlations were computed using the *dcor* package in Python (https://dcor.readthedocs.io/en/latest/index.html). These results are displayed in **Supplementary Figure 5**.

Multi-Set Canonical Correlation Analysis

To estimate the *joint* fluctuations between physiological and the first principal component time courses, we implemented a multi-set canonical correlation analysis (MCCA) on the full set of signals in each dataset. Each 'set' corresponds to the lag spline basis (see below) of a single electrophysiological signal (positive lag of ~10s; N = 3 splines). The objective is to find a linear-weighted combination of the time-lagged copies of each signal that maximizes the pairwise correlations between all signals. MCCA was performed at the group-level by group-wise temporal concenation We extract the first canonical component from the MCCA algorithm, corresponding to the linear weighted combination of all signals that produces the maximum pairwise correlation between signals. The MCCA algorithm was implemented in the cca-zoo Python package (https://github.com/jameschapman19/cca_zoo). Illustration of the MCCA approach used in our study is provided in **Supplementary Figure 9**.

Statistical significance testing of the average pairwise correlation of the first canonical component was performed using block-wise permutation of subject time courses before temporal concatenation across subjects. Specifically, for each signal (physiological signals and first principal component), subject time courses were randomly reordered before temporal concatenation to preserve the time course structure within subjects. Once performed across all signals, this permutation procedure eliminates the relationships across temporally concatenated signals, while preserving the autocorrelation structure within each signal. For example, one

permutation may align signal A in subject 1, with signal B in subject 7, and so forth. For each permutation (N=1000), the average pairwise correlation between all permuted time courses of the first canonical component was extracted to construct a null distribution.

Explained Variance of Spontaneous Global BOLD Fluctuations By Respiration Rate and Depth

One interest of this study was the separate contributions of respiration rate and respiration depth/amplitude to spontaneous fluctuations in global BOLD fluctuations. We performed subject-level variance partitioning analysis of respiration rate and depth regressed onto the first principal component time course (**Figure 2C**). Sometimes referred to as commonality analysis (Seibold & McPhee, 1979), this approach decomposes the total variance explained by both respiration rate and respiration depth into 1) the unique variance explained by each and 2) the variance explained in common. Our implementation of the approach involved estimating ordinary least squares regression models with either respiration rate or respiration depth (and their time lags) left out of the model. Note, time lags were incorporated using a spline basis (see below) over time lags of the original signal (positive lag of ~10s; N = 3 splines). Subtraction of the total explained variance from the explained variance derived from the regression model with respiration rate left out provides the unique variance explained by respiration rate. Subtraction of the total variance by the unique explained variance of both respiration rate and respiration depth provides an estimate of the common variance explained by both signals. This analysis was performed for each subject across all three resting-state datasets (ME-REST, HCP-REST, and ME-REST-SUPP).

Non-Linear Modeling of Hemodynamic Response to Respiration Fluctuations

To estimate the hemodynamic response to respiratory volume fluctuations across the brain, CSF and white matter, we utilized a mass-univariate distributed lag non-linear model (DLNLM) (Gasparrini et al., 2010). This analysis was performed on the ME-REST, HCP-REST and ME-REST-SUPP datasets. This approach was used to model both the time-lag response and potential non-linearities in the response at different levels of respiratory volume at each voxel. As opposed to a-priori hemodynamic response functions, this approach allowed a data-driven approach to estimating the hemodynamic response distributed over a pre-specified time window. For each electrophysiological signal, time-lagged predictors were generated via linear combination of time-lagged copies of the signal with a natural cubic spline basis with five cubic splines equally spaced across the time window (from -n to n time points). The resulting time-lagged predictor is represented by five linear-weighted versions of the original signal encoding a smooth curve across the time window. For the ME-REST dataset, the time window extended from -5 (10s) to 15 TRs (31.5s). For the HCP-REST dataset, the time window extended from -14 (10s) to 45 TRs (32.4s). For the ME-REST-SUPP dataset, the time window extended from -4 (12s) to 10 TRs (30s). Negative lags were included to ensure that BOLD responses captured the start of inspiration, not just the peaks of respiratory volume (i.e. points where inhalation

ended and exhalation began). As we show in **Figure 4**, the inclusion of negative lags captures the overshoot phase of the respiration response, in line with task-based trial-averaging of hemodynamic responses indexed to the start of inspiration.

This lag spline basis is combined with a natural cubic spline basis in the space of the respiratory volume time courses (number of splines = 6). Without the lag spline basis, this approach would reduce to conventional additive models with a spline basis (Buja et al., 1989). For intuition, if one envisions time-lagged copies of respiration amplitude signals from -N to *N* TRs forming columns of a two-dimensional matrix, a spline basis over the columns (i.e. the time-lag) would correspond to the lag spline basis, and the spline basis over the rows (i.e. the values of the respiratory volume signal across time) would form the spline basis in the space of the respiration volume signals. The DLNM model estimates effects that vary simultaneously along the time-lag and predictor signal space by constructing a cross-basis matrix between the two spline bases (i.e. the lag spline basis and the spline basis in the space of the predictor). Specifically, the cross-basis matrix is formed from the tensor product between the two spline bases, in the same manner that tensor product smooths are implemented in conventional additive (or generalized additive) models. An illustration of the DLNM model approach is provided in **Supplementary Figure 8**.

The model was estimated with ordinary least squares at each voxel. To evaluate the hemodynamic response to respiratory volume fluctuations from the model, we computed the predicted BOLD time course over the time window (-N to *N* TRs) at each voxel. We evaluated the predicted BOLD response at each voxel to a range of positive respiratory volume value (0.5 - 2.5 in z-score units). A global average hemodynamic response was constructed by averaging the predicted BOLD response across all gray matter voxels over the time window. The shapes of the global average response at different values of respiratory volume were examined to assess potential non-linearities in the hemodynamic response.

Vigilance Modulation of Global BOLD Signal Amplitudes and Covariation with Respiratory Time Courses

To examine variation in the amplitude of global BOLD and CSF fluctuations over resting-state fMRI scanning sessions, and how they are related to participant vigilance states, we analyzed data from the multi-echo simultaneous EEG-fMRI resting-state dataset (ME-REST; **Figure 3**) To estimate variation in the amplitude of global BOLD and CSF fluctuations we computed sliding window variance time courses from global BOLD/CSF signals using a rectangular window of 50 time samples (105s). To estimate low-frequency vigilance states we computed sliding window average time courses from the EEG-derived vigilance index using the same sliding window parameters. To assess robustness of our results across window sizes, we re-analyzed our findings with window sizes ranging from 20 (42s) - 80 (168s) time points and the results were found to be stable across window sizes (**Figure 3**).

To determine whether the relationship between respiratory volume and global BOLD signals were modulated by vigilance state, we conducted a regression analysis with global

BOLD time courses regressed on respiratory volume time courses and the sliding window vigilance index, and their interaction term. The regression was performed at the group level on temporally-concatenated global BOLD, respiratory volume and vigilance time courses signals across subjects. For statistical inference, we utilized a generalized estimating equation (GEE) approach to correct standard error estimates for clustering within subjects. Autocorrelation in the electrophysiological signals were accounted for by the inclusion of a first-order autoregressive covariance structure. Note, global BOLD time courses and respiratory volume signals were z-scored before concatenation.

Respiration Task Event Averages

Event-related averaging of the ME-TASK and NKI-TASK datasets was performed to examine the hemodynamic and physiological response to deep breaths and breath holds. For the ME-TASK, group-level response functions for each electrophysiological signals were generated by the following procedure: 1) subject-level response functions were generated by averaging the physiological time courses from each trial (starting from onset out to ~29s), 2) subject-level response functions were then averaged across subjects to obtain a group-averaged response function. For the NKI-TASK dataset, subject-level physiological time courses were averaged across subjects to generate a scan-averaged time course.

For the ME-TASK dataset, event-related EEG power fluctuations were examined for each subject by averaging Wavelet filter bank power signals (i.e. time-frequency spectral power in 2-20Hz frequencies; see above) within a 20s window post breath-onset across trials. Baseline log-ratio normalization (i.e. decibels) was applied to the subject-averaged time courses with the time span 1s before up until stimulus onset as the baseline. A group event-related average was constructed from averaging across event-related subject averages.

References

Allen, P. J., Josephs, O., & Turner, R. (2000). A Method for Removing Imaging Artifact from Continuous EEG Recorded during Functional MRI. *NeuroImage*, *12*(2), 230–239.

https://doi.org/10.1006/nimg.2000.0599

Andersson, J., Jenkinson, M., & Smith, S. (2010). Non-linear registration, aka spatial normalization. *FMRIB Technical Report TR07JA2*.

Bini, G., Hagbarth, K. E., Hynninen, P., & Wallin, B. G. (1980). Thermoregulatory and rhythm-generating mechanisms governing the sudomotor and vasoconstrictor outflow in human cutaneous nerves. *The Journal of Physiology*, *306*, 537–552. https://doi.org/10.1113/jphysiol.1980.sp013413

Birn, R. M., Smith, M. A., Jones, T. B., & Bandettini, P. A. (2008). The Respiration Response Function: The temporal dynamics of fMRI signal fluctuations related to changes in respiration. *NeuroImage*, *40*(2), 644–654. https://doi.org/10.1016/j.neuroimage.2007.11.059

Bolt, T., Nomi, J. S., Bzdok, D., Salas, J. A., Chang, C., Thomas Yeo, B. T., Uddin, L. Q., & Keilholz, S. D. (2022). A parsimonious description of global functional brain organization in three spatiotemporal patterns. *Nature Neuroscience*, *25*(8), Article 8. https://doi.org/10.1038/s41593-022-01118-1

Buja, A., Hastie, T., & Tibshirani, R. (1989). Linear Smoothers and Additive Models. *The Annals of Statistics*, *17*(2), 453–510. https://doi.org/10.1214/aos/1176347115

Buxton, R. B., Uludağ, K., Dubowitz, D. J., & Liu, T. T. (2004). Modeling the hemodynamic response to brain activation. *NeuroImage*, *23*, S220–S233. https://doi.org/10.1016/j.neuroimage.2004.07.013

Chang, C., Cunningham, J. P., & Glover, G. H. (2009). Influence of heart rate on the BOLD signal: The cardiac response function. *NeuroImage*, *44*(3), 857–869. https://doi.org/10.1016/j.neuroimage.2008.09.029

Chang, C., & Glover, G. H. (2009). Relationship between respiration, end-tidal CO2, and BOLD signals in resting-state fMRI. *NeuroImage*, *47*(4), 1381–1393. https://doi.org/10.1016/j.neuroimage.2009.04.048

de Munck, J. C., Gonçalves, S. I., Faes, T. J. C., Kuijer, J. P. A., Pouwels, P. J. W., Heethaar, R. M., & Lopes da Silva, F. H. (2008). A study of the brain's resting state based on alpha band power, heart rate and fMRI. *NeuroImage*, *42*(1), 112–121. https://doi.org/10.1016/j.neuroimage.2008.04.244

DuPre, E., Salo, T., Markello, R., Kundu, P., Whitaker, K., & Handwerker, D. (2020). *ME-ICA/tedana: 0.0.9a*. Zenodo. https://doi.org/10.5281/zenodo.3786890

Elgendi, M., Norton, I., Brearley, M., Abbott, D., & Schuurmans, D. (2013). Systolic peak detection in acceleration photoplethysmograms measured from emergency responders in tropical conditions. *PloS One*, *8*(10), e76585. https://doi.org/10.1371/journal.pone.0076585

Falahpour, M., Chang, C., Wong, C. W., & Liu, T. T. (2018). Template-based prediction of vigilance fluctuations in resting-state fMRI. *NeuroImage*, *174*, 317–327. https://doi.org/10.1016/j.neuroimage.2018.03.012

Fan, J., Xu, P., Van Dam, N. T., Eilam-Stock, T., Gu, X., Luo, Y., & Hof, P. R. (2012). Spontaneous Brain Activity Relates to Autonomic Arousal. *The Journal of Neuroscience*, *32*(33), 11176–11186. https://doi.org/10.1523/JNEUROSCI.1172-12.2012

Fox, M. D., & Raichle, M. E. (2007). Spontaneous fluctuations in brain activity observed with functional magnetic resonance imaging. *Nature Reviews Neuroscience*, *8*(9), Article 9. https://doi.org/10.1038/nrn2201

Fritsch, F. N., & Butland, J. (1984). A Method for Constructing Local Monotone Piecewise Cubic Interpolants. *SIAM Journal on Scientific and Statistical Computing*, *5*(2), 300–304. https://doi.org/10.1137/0905021

Fultz, N. E., Bonmassar, G., Setsompop, K., Stickgold, R. A., Rosen, B. R., Polimeni, J. R., & Lewis, L. D. (2019). Coupled electrophysiological, hemodynamic, and cerebrospinal fluid oscillations in human sleep. *Science*, *366*(6465), 628–631. https://doi.org/10.1126/science.aax5440

Gasparrini, A., Armstrong, B., & Kenward, M. G. (2010). Distributed lag non-linear models. *Statistics in Medicine*, *29*(21), 2224–2234. https://doi.org/10.1002/sim.3940

Gertler, J., Novotny, S., Poppe, A., Chung, Y. S., Gross, J. J., Pearlson, G., & Stevens, M. C. (2020). Neural correlates of non-specific skin conductance responses during resting state fMRI. *NeuroImage*, *214*, 116721. https://doi.org/10.1016/j.neuroimage.2020.116721

Glasser, M. F., Sotiropoulos, S. N., Wilson, J. A., Coalson, T. S., Fischl, B., Andersson, J. L., Xu, J., Jbabdi, S., Webster, M., Polimeni, J. R., Van Essen, D. C., Jenkinson, M., & WU-Minn HCP Consortium. (2013). The minimal preprocessing pipelines for the Human Connectome Project. *NeuroImage*, *80*, 105–124. https://doi.org/10.1016/j.neuroimage.2013.04.127

Gonzalez-Castillo, J., Fernandez, I. S., Handwerker, D. A., & Bandettini, P. A. (2022). Ultra-slow fMRI fluctuations in the fourth ventricle as a marker of drowsiness. *NeuroImage*, *259*, 119424. https://doi.org/10.1016/j.neuroimage.2022.119424

Goodale, S. E., Ahmed, N., Zhao, C., de Zwart, J. A., Özbay, P. S., Picchioni, D., Duyn, J., Englot, D. J., Morgan, V. L., & Chang, C. (2021). FMRI-based detection of alertness predicts behavioral response variability. *ELife*, *10*, e62376. https://doi.org/10.7554/eLife.62376

Gramfort, A., Luessi, M., Larson, E., Engemann, D., Strohmeier, D., Brodbeck, C., Goj, R., Jas, M., Brooks, T., Parkkonen, L., & Hämäläinen, M. (2013). MEG and EEG data analysis with MNE-Python. *Frontiers in Neuroscience*, *7*. https://www.frontiersin.org/articles/10.3389/fnins.2013.00267

Gu, Y., Han, F., Sainburg, L. E., Schade, M. M., Buxton, O. M., Duyn, J. H., & Liu, X. (2022). An orderly sequence of autonomic and neural events at transient arousal changes. *NeuroImage*, *264*, 119720. https://doi.org/10.1016/j.neuroimage.2022.119720

Häbler, H.-J., Jänig, W., & Michaelis, M. (1994). Respiratory modulation in the activity of

sympathetic neurones. *Progress in Neurobiology*, *43*(6), 567–606. https://doi.org/10.1016/0301-0082(94)90053-1

Hamner, J. w., Tan, C. O., Lee, K., Cohen, M. A., & Taylor, J. A. (2010). Sympathetic Control of the Cerebral Vasculature in Humans. *Stroke*, *41*(1), 102–109. https://doi.org/10.1161/STROKEAHA.109.557132

Harrison, S. J., Bianchi, S., Heinzle, J., Stephan, K. E., Iglesias, S., & Kasper, L. (2021). A Hilbert-based method for processing respiratory timeseries. *NeuroImage*, *230*, 117787. https://doi.org/10.1016/j.neuroimage.2021.117787

Heck, D. H., McAfee, S. S., Liu, Y., Babajani-Feremi, A., Rezaie, R., Freeman, W. J., Wheless, J. W., Papanicolaou, A. C., Ruszinkó, M., Sokolov, Y., & Kozma, R. (2017). Breathing as a Fundamental Rhythm of Brain Function. *Frontiers in Neural Circuits*, *10*. https://www.frontiersin.org/articles/10.3389/fncir.2016.00115

Herrero, J. L., Khuvis, S., Yeagle, E., Cerf, M., & Mehta, A. D. (2018). Breathing above the brain stem: Volitional control and attentional modulation in humans. *Journal of Neurophysiology*, *119*(1), 145–159. https://doi.org/10.1152/jn.00551.2017

Ito, J., Roy, S., Liu, Y., Cao, Y., Fletcher, M., Lu, L., Boughter, J. D., Grün, S., & Heck, D. H. (2014). Whisker barrel cortex delta oscillations and gamma power in the awake mouse are linked to respiration. *Nature Communications*, *5*(1), 3572. https://doi.org/10.1038/ncomms4572

Jänig, W., Kümmel, H., & Wiprich, L. (1980). Respiratory Rhythmicities in Vasoconstrictor and Sudomotor Neurones Supplying the Cat's Hindlimb. In H. P. Koepchen, S. M. Hilton, & A. Trzebski (Eds.), *Central Interaction Between Respiratory and Cardiovascular Control Systems* (pp. 128–136). Springer. https://doi.org/10.1007/978-3-642-67603-1_15

Johnson, L. C., & Lubin, A. (1967). The orienting reflex during waking and sleeping. *Electroencephalography and Clinical Neurophysiology*, *22*(1), 11–21. https://doi.org/10.1016/0013-4694(67)90004-1

Karalis, N., & Sirota, A. (2022). Breathing coordinates cortico-hippocampal dynamics in mice during offline states. *Nature Communications*, *13*(1), Article 1. https://doi.org/10.1038/s41467-022-28090-5

Kay, K., Jamison, K. W., Zhang, R.-Y., & Uğurbil, K. (2020). A temporal decomposition method for identifying venous effects in task-based fMRI. *Nature Methods*, *17*(10), Article 10. https://doi.org/10.1038/s41592-020-0941-6

Khoo, M. C. K., & Chalacheva, P. (2019). Respiratory modulation of peripheral vasoconstriction: A modeling perspective. *Journal of Applied Physiology*, *127*(5), 1177–1186. https://doi.org/10.1152/japplphysiol.00111.2019

Kluger, D. S., Balestrieri, E., Busch, N. A., & Gross, J. (2021). Respiration aligns perception with neural excitability. *ELife*, *10*, e70907. https://doi.org/10.7554/eLife.70907

Kluger, D. S., & Gross, J. (2021). Respiration modulates oscillatory neural network activity at rest. *PLOS Biology*, *19*(11), e3001457. https://doi.org/10.1371/journal.pbio.3001457

Koep, J. L., Taylor, C. E., Coombes, J. S., Bond, B., Ainslie, P. N., & Bailey, T. G. (2022). Autonomic control of cerebral blood flow: Fundamental comparisons between peripheral and cerebrovascular circulations in humans. *The Journal of Physiology*, *600*(1), 15–39. https://doi.org/10.1113/JP281058

Kundu, P., Brenowitz, N. D., Voon, V., Worbe, Y., Vértes, P. E., Inati, S. J., Saad, Z. S., Bandettini, P. A., & Bullmore, E. T. (2013). Integrated strategy for improving functional connectivity mapping using multiecho fMRI. *Proceedings of the National Academy of Sciences*, *110*(40), 16187–16192. https://doi.org/10.1073/pnas.1301725110

Kundu, P., Santin, M. D., Bandettini, P. A., Bullmore, E. T., & Petiet, A. (2014). Differentiating BOLD and non-BOLD signals in fMRI time series from anesthetized rats using multi-echo EPI at 11.7T. *NeuroImage*, *102*, 861–874. https://doi.org/10.1016/j.neuroimage.2014.07.025

Lee, K., Horien, C., O'Connor, D., Garand-Sheridan, B., Tokoglu, F., Scheinost, D., Lake, E. M.

R., & Constable, R. T. (2022). Arousal impacts distributed hubs modulating the integration of brain functional connectivity. *NeuroImage*, *258*, 119364. https://doi.org/10.1016/j.neuroimage.2022.119364

Li, J., Bolt, T., Bzdok, D., Nomi, J. S., Yeo, B. T. T., Spreng, R. N., & Uddin, L. Q. (2019). Topography and behavioral relevance of the global signal in the human brain. *Scientific Reports*, *9*(1), Article 1. https://doi.org/10.1038/s41598-019-50750-8

Liu, T. T., Nalci, A., & Falahpour, M. (2017). The Global Signal in fMRI: Nuisance or Information? *NeuroImage*, *150*, 213–229. https://doi.org/10.1016/j.neuroimage.2017.02.036

Lykken, D. T., & Venables, P. H. (1971). Direct Measurement of Skin Conductance: A Proposal for Standardization. *Psychophysiology*, *8*(5), 656–672. https://doi.org/10.1111/j.1469-8986.1971.tb00501.x

Malpas, S. C. (2010). Sympathetic nervous system overactivity and its role in the development of cardiovascular disease. *Physiological Reviews*, *90*(2), 513–557. https://doi.org/10.1152/physrev.00007.2009

Markiewicz, C. J., Gorgolewski, K. J., Feingold, F., Blair, R., Halchenko, Y. O., Miller, E., Hardcastle, N., Wexler, J., Esteban, O., Goncavles, M., Jwa, A., & Poldrack, R. (2021). The OpenNeuro resource for sharing of neuroscience data. *ELife*, *10*, e71774. https://doi.org/10.7554/eLife.71774

Marumo, C., & Nakano, T. (2021). Early phase of pupil dilation is mediated by the peripheral parasympathetic pathway. *Journal of Neurophysiology*, *126*(6), 2130–2137. https://doi.org/10.1152/jn.00401.2021

Menon, R. S. (2002). Postacquisition suppression of large-vessel BOLD signals in high-resolution fMRI. *Magnetic Resonance in Medicine*, *47*(1), 1–9. https://doi.org/10.1002/mrm.10041

Moore, C. I., & Cao, R. (2008). The Hemo-Neural Hypothesis: On The Role of Blood Flow in

Information Processing. *Journal of Neurophysiology*, *99*(5), 2035–2047. https://doi.org/10.1152/jn.01366.2006

Murphy, K., Birn, R. M., Handwerker, D. A., Jones, T. B., & Bandettini, P. A. (2009). The impact of global signal regression on resting state correlations: Are anti-correlated networks introduced? *NeuroImage*, *44*(3), 893–905. https://doi.org/10.1016/j.neuroimage.2008.09.036

Nagai, Y., Critchley, H. D., Featherstone, E., Trimble, M. R., & Dolan, R. J. (2004). Activity in ventromedial prefrontal cortex covaries with sympathetic skin conductance level: A physiological account of a “default mode” of brain function. *NeuroImage*, *22*(1), 243–251. https://doi.org/10.1016/j.neuroimage.2004.01.019

Nakada, K., Yoshida, D., Fukumoto, M., & Yoshida, S. (2001). Chronological analysis of physiological T2* signal change in the cerebrum during breath holding. *Journal of Magnetic Resonance Imaging*, *13*(3), 344–351. https://doi.org/10.1002/jmri.1049

Nooner, K., Colcombe, S., Tobe, R., Mennes, M., Benedict, M., Moreno, A., Panek, L., Brown, S., Zavitz, S., Li, Q., Sikka, S., Gutman, D., Bangaru, S., Schlachter, R. T., Kamiel, S., Anwar, A., Hinz, C., Kaplan, M., Rachlin, A., … Milham, M. (2012). The NKI-Rockland Sample: A Model for Accelerating the Pace of Discovery Science in Psychiatry. *Frontiers in Neuroscience*, *6*. https://www.frontiersin.org/articles/10.3389/fnins.2012.00152

Obrig, H., Neufang, M., Wenzel, R., Kohl, M., Steinbrink, J., Einhäupl, K., & Villringer, A. (2000). Spontaneous low frequency oscillations of cerebral hemodynamics and metabolism in human adults. *NeuroImage*, *12*(6), 623–639. https://doi.org/10.1006/nimg.2000.0657

Ohtsuka, K., Asakura, K., Kawasaki, H., & Sawa, M. (1988). Respiratory fluctuations of the human pupil. *Experimental Brain Research*, *71*(1), 215–217. https://doi.org/10.1007/BF00247537

Özbay, P. S., Chang, C., Picchioni, D., Mandelkow, H., Chappel-Farley, M. G., van Gelderen, P., de Zwart, J. A., & Duyn, J. (2019). Sympathetic activity contributes to the fMRI signal.

Communications Biology, *2*(1), 1–9. https://doi.org/10.1038/s42003-019-0659-0

Pais-Roldán, P., Takahashi, K., Sobczak, F., Chen, Y., Zhao, X., Zeng, H., Jiang, Y., & Yu, X. (2020). Indexing brain state-dependent pupil dynamics with simultaneous fMRI and optical fiber calcium recording. *Proceedings of the National Academy of Sciences of the United States of America*, *117*(12), 6875–6882. https://doi.org/10.1073/pnas.1909937117

Panerai, R. B., Simpson, D. M., Deverson, S. T., Mahony, P., Hayes, P., & Evans, D. H. (2000). Multivariate dynamic analysis of cerebral blood flow regulation in humans. *IEEE Transactions on Bio-Medical Engineering*, *47*(3), 419–423. https://doi.org/10.1109/10.827312

Pereira, A., & Furlan, F. A. (2010). Astrocytes and human cognition: Modeling information integration and modulation of neuronal activity. *Progress in Neurobiology*, *92*(3), 405–420. https://doi.org/10.1016/j.pneurobio.2010.07.001

Picchioni, D., Özbay, P. S., Mandelkow, H., de Zwart, J. A., Wang, Y., van Gelderen, P., & Duyn, J. H. (2022). Autonomic arousals contribute to brain fluid pulsations during sleep. *NeuroImage*, *249*, 118888. https://doi.org/10.1016/j.neuroimage.2022.118888

Power, J. D., Plitt, M., Laumann, T. O., & Martin, A. (2017). Sources and implications of whole-brain fMRI signals in humans. *NeuroImage*, *146*, 609–625. https://doi.org/10.1016/j.neuroimage.2016.09.038

Raut, R. V., Snyder, A. Z., Mitra, A., Yellin, D., Fujii, N., Malach, R., & Raichle, M. E. (2021). Global waves synchronize the brain's functional systems with fluctuating arousal. *Science Advances*, *7*(30), eabf2709. https://doi.org/10.1126/sciadv.abf2709

Samuels, E. R., & Szabadi, E. (2008). Functional Neuroanatomy of the Noradrenergic Locus Coeruleus: Its Roles in the Regulation of Arousal and Autonomic Function Part II: Physiological and Pharmacological Manipulations and Pathological Alterations of Locus Coeruleus Activity in Humans. *Current Neuropharmacology*, *6*(3), 254–285.

https://doi.org/10.2174/157015908785777193

Schölvinck, M. L., Maier, A., Ye, F. Q., Duyn, J. H., & Leopold, D. A. (2010). Neural basis of global resting-state fMRI activity. *Proceedings of the National Academy of Sciences*, *107*(22), 10238–10243. https://doi.org/10.1073/pnas.0913110107

Seibold, D. R., & McPhee, R. D. (1979). Commonality Analysis: A Method for Decomposing Explained Variance in Multiple Regression Analyses. *Human Communication Research*, *5*(4), 355–365. https://doi.org/10.1111/j.1468-2958.1979.tb00649.x

Setton, R., Mwilambwe-Tshilobo, L., Girn, M., Lockrow, A. W., Baracchini, G., Hughes, C., Lowe, A. J., Cassidy, B. N., Li, J., Luh, W.-M., Bzdok, D., Leahy, R. M., Ge, T., Margulies, D. S., Misic, B., Bernhardt, B. C., Stevens, W. D., De Brigard, F., Kundu, P., … Spreng, R. N. (2023). Age differences in the functional architecture of the human brain. *Cerebral Cortex*, *33*(1), 114–134. https://doi.org/10.1093/cercor/bhac056

Shams, S., LeVan, P., & Chen, J. J. (2021). The neuronal associations of respiratory-volume variability in the resting state. *NeuroImage*, *230*, 117783. https://doi.org/10.1016/j.neuroimage.2021.117783

Shmueli, K., van Gelderen, P., de Zwart, J. A., Horovitz, S. G., Fukunaga, M., Jansma, J. M., & Duyn, J. H. (2007). Low-frequency fluctuations in the cardiac rate as a source of variance in the resting-state fMRI BOLD signal. *NeuroImage*, *38*(2), 306–320. https://doi.org/10.1016/j.neuroimage.2007.07.037

Smith, S. M., Andersson, J., Auerbach, E. J., Beckmann, C. F., Bijsterbosch, J., Douaud, G., Duff, E., Feinberg, D. A., Griffanti, L., Harms, M. P., Kelly, M., Laumann, T., Miller, K. L., Moeller, S., Petersen, S., Power, J., Salimi-Khorshidi, G., Snyder, A. Z., Vu, A., … Glasser, M. F. (2013). Resting-state fMRI in the Human Connectome Project. *NeuroImage*, *80*, 144–168. https://doi.org/10.1016/j.neuroimage.2013.05.039

Sokolov, E. N. (1963). Higher Nervous Functions: The Orienting Reflex. *Annual Review of Physiology*, *25*(1), 545–580. https://doi.org/10.1146/annurev.ph.25.030163.002553

Soon, C. S., Vinogradova, K., Ong, J. L., Calhoun, V. D., Liu, T., Zhou, J. H., Ng, K. K., & Chee, M. W. L. (2021). Respiratory, cardiac, EEG, BOLD signals and functional connectivity over multiple microsleep episodes. *NeuroImage*, *237*, 118129. https://doi.org/10.1016/j.neuroimage.2021.118129

Spreng, R. N., Setton, R., Alter, U., Cassidy, B. N., Darboh, B., DuPre, E., Kantarovich, K., Lockrow, A. W., Mwilambwe-Tshilobo, L., Luh, W.-M., Kundu, P., & Turner, G. R. (2022). Neurocognitive aging data release with behavioral, structural and multi-echo functional MRI measures. *Scientific Data*, *9*(1), Article 1. https://doi.org/10.1038/s41597-022-01231-7

Székely, G. J., Rizzo, M. L., & Bakirov, N. K. (2007). Measuring and testing dependence by correlation of distances. *The Annals of Statistics*, *35*(6), 2769–2794. https://doi.org/10.1214/009053607000000505

Tong, Y., Hocke, L. M., Licata, S. C., & deB. Frederick, B. (2012). Low-frequency oscillations measured in the periphery with near-infrared spectroscopy are strongly correlated with blood oxygen level-dependent functional magnetic resonance imaging signals. *Journal of Biomedical Optics*, *17*(10), 106004. https://doi.org/10.1117/1.JBO.17.10.106004

Tu, W., & Zhang, N. (2022). Neural underpinning of a respiration-associated resting-state fMRI network. *ELife*, *11*, e81555. https://doi.org/10.7554/eLife.81555

Uddin, L. Q. (2017). Mixed Signals: On Separating Brain Signal from Noise. *Trends in Cognitive Sciences*, *21*(6), 405–406. https://doi.org/10.1016/j.tics.2017.04.002

Uddin, L. Q. (2020). Bring the Noise: Reconceptualizing Spontaneous Neural Activity. *Trends in Cognitive Sciences*, *24*(9), 734–746. https://doi.org/10.1016/j.tics.2020.06.003

Van Essen, D. C., Smith, S. M., Barch, D. M., Behrens, T. E. J., Yacoub, E., Ugurbil, K., & WU-Minn HCP Consortium. (2013). The WU-Minn Human Connectome Project: An overview. *NeuroImage*, *80*, 62–79. https://doi.org/10.1016/j.neuroimage.2013.05.041

van Lieshout, J. J., & Secher, N. H. (2008). Point:Counterpoint: Sympathetic activity does/does

not influence cerebral blood flow. *Journal of Applied Physiology*, *105*(4), 1364–1366. https://doi.org/10.1152/japplphysiol.90597.2008

Viviani, R. (2016). A Digital Atlas of Middle to Large Brain Vessels and Their Relation to Cortical and Subcortical Structures. *Frontiers in Neuroanatomy*, *10*. https://www.frontiersin.org/articles/10.3389/fnana.2016.00012

Ward, P. G. D., Ferris, N. J., Raniga, P., Dowe, D. L., Ng, A. C. L., Barnes, D. G., & Egan, G. F. (2018). Combining images and anatomical knowledge to improve automated vein segmentation in MRI. *NeuroImage*, *165*, 294–305. https://doi.org/10.1016/j.neuroimage.2017.10.049

Wen, H., & Liu, Z. (2016). Broadband Electrophysiological Dynamics Contribute to Global Resting-State fMRI Signal. *The Journal of Neuroscience: The Official Journal of the Society for Neuroscience*, *36*(22), 6030–6040. https://doi.org/10.1523/JNEUROSCI.0187-16.2016

Wise, R. G., Ide, K., Poulin, M. J., & Tracey, I. (2004). Resting fluctuations in arterial carbon dioxide induce significant low frequency variations in BOLD signal. *NeuroImage*, *21*(4), 1652–1664. https://doi.org/10.1016/j.neuroimage.2003.11.025

Wong, C. W., Olafsson, V., Tal, O., & Liu, T. T. (2013). The amplitude of the resting-state fMRI global signal is related to EEG vigilance measures. *NeuroImage*, *83*, 983–990. https://doi.org/10.1016/j.neuroimage.2013.07.057

Yasuma, F., & Hayano, J.-I. (2004). Respiratory sinus arrhythmia: Why does the heartbeat synchronize with respiratory rhythm? *Chest*, *125*(2), 683–690. https://doi.org/10.1378/chest.125.2.683

Yellin, D., Berkovich-Ohana, A., & Malach, R. (2015). Coupling between pupil fluctuations and resting-state fMRI uncovers a slow build-up of antagonistic responses in the human cortex. *NeuroImage*, *106*, 414–427. https://doi.org/10.1016/j.neuroimage.2014.11.034

Yuan, H., Zotev, V., Phillips, R., & Bodurka, J. (2013). Correlated slow fluctuations in

respiration, EEG, and BOLD fMRI. *NeuroImage*, *79*, 81–93. https://doi.org/10.1016/j.neuroimage.2013.04.068

Zelano, C., Jiang, H., Zhou, G., Arora, N., Schuele, S., Rosenow, J., & Gottfried, J. A. (2016). Nasal Respiration Entrains Human Limbic Oscillations and Modulates Cognitive Function. *Journal of Neuroscience*, *36*(49), 12448–12467. https://doi.org/10.1523/JNEUROSCI.2586-16.2016

Zhang, Y., Brady, M., & Smith, S. (2001). Segmentation of brain MR images through a hidden Markov random field model and the expectation-maximization algorithm. *IEEE Transactions on Medical Imaging*, *20*(1), 45–57. https://doi.org/10.1109/42.906424